ANNUAL REVIEWS

Annual Review of Materials Research

Insights into Plastic Localization by Crystallographic Slip from Emerging Experimental and Numerical Approaches

J.C. Stinville,[1] M.A. Charpagne,[1] R. Maaß,[1,2] H. Proudhon,[3] W. Ludwig,[4,5] P.G. Callahan,[6] F. Wang,[7] I.J. Beyerlein,[8] M.P. Echlin,[8] and T.M. Pollock[8]

[1]Department of Materials Science and Engineering, University of Illinois Urbana-Champaign, Urbana, Illinois, USA

[2]Federal Institute of Materials Research and Testing (BAM), Berlin, Germany

[3]Centre for Material Sciences (MAT), UMR7633CNRS, MINESParis, PSL University, Evry, France

[4]MATEIS INSA Lyon, CNRS UMR 5510, University of Lyon I, Villeurbanne, France

[5]European Synchrotron Radiation Facility, Grenoble, France

[6]Materials Science and Technology Division, US Naval Research Laboratory, Washington, DC, USA

[7]National Engineering Research Center of Light Alloy Net Forming, School of Materials Science and Engineering, Shanghai Jiao Tong University, Shanghai, China

[8]Materials Department, University California, Santa Barbara, California, USA; email: mechlin@ucsb.edu

Annu. Rev. Mater. Res. 2023. 53:275–317

The *Annual Review of Materials Research* is online at matsci.annualreviews.org

https://doi.org/10.1146/annurev-matsci-080921-102621

Keywords

slip localization, metallic materials, experimental and numerical techniques, mechanical properties, plasticity

Abstract

Advanced experimental and numerical approaches are being developed to capture the localization of plasticity at the nanometer scale as a function of the multiscale and heterogeneous microstructure present in metallic materials. These innovative approaches promise new avenues to understand microstructural effects on mechanical properties, accelerate alloy design, and enable more accurate mechanical property prediction. This article provides an overview of emerging approaches with a focus on the localization of

plasticity by crystallographic slip. New insights into the mechanisms and mechanics of strain localization are addressed. The consequences of the localization of plasticity by deformation slip for mechanical properties of metallic materials are also detailed.

1. INTRODUCTION

Rapidly evolving economic, social, and political driving forces demand improvements in the environmental impact, safety, reliability, affordability, sustainability, and efficiency of advanced engineering systems. Metallic materials are at the core of many of these systems and their multiscale, hierarchical microstructures have made predicting their properties and performance elusive for decades. Prediction of mechanical properties is challenging due to gaps in understanding the spatial and temporal heterogeneity of the crystallographic slip processes that determine these properties. Particularly challenging are the microstructures introduced by advanced manufacturing processes (e.g., 3D printing) and the complex deformation mechanisms present in materials that perform in extreme environments (e.g., very high temperature, cryogenic temperature, long-term mechanical behavior, exposure to hydrogen or liquid hydrogen). However, recent innovative experimental tools coupled with emerging computational techniques promise significant strides in our predictive capabilities. These innovations may fundamentally change how new materials are developed and integrated within the systems design process, accelerating the time from design to production and enabling accurate prediction of the life of critical components.

The new experimental and numerical tools reviewed here are being developed to characterize and more accurately predict the effect of microstructures on mechanical properties in advanced engineering materials. Recent innovations in rapid, automated characterization over large 2D and 3D volumes at increasingly higher resolution enable statistical assessment of the connection between local plasticity at the nanometer scale to the microstructure at the millimeter scale. On the experimental side, these tools include high-resolution digital image correlation (HR-DIC) in the scanning electron microscope (SEM) (1, 2), automated nanoindentation (3), high-throughput mechanical testing of miniaturized specimens (4–6), high-speed atomic force microscopy (AFM) (7), high-speed electron backscatter diffraction (EBSD), X-ray topotomography (TT) (8, 9) or dark-field X-ray microscopy (DFXM) (10), and transmission scanning electron microscopy (TSEM) (11). They all capture a physical signature of the deformation process over large surface areas or volumes. For instance, slip extrusions are measured using high-speed AFM and in-plane slip displacements are measured using HR-DIC. Some of these experimental methods probe representative areas or volumes of the microstructure by examining signatures of the deformation processes over large specimens or by testing a large number of miniaturized specimens using so-called high-throughput testing (12). On the numerical side, significant achievements have been made due to advances in computational power. It is now possible to perform large-scale calculations over cubic millimeter–scaled microstructures while modeling the deformation processes at the submicrometer scale. The recent development of massively parallel fast Fourier transformation (FFT)-based calculations has provided the opportunity to perform simulations that capture the 3D complexity of the grain structure while explicitly describing the deformation processes (13).

Along with these innovative measurements, new approaches have emerged for the automation of data acquisition, reconstruction, and merging (fusion) of multimodal data sets, potentially from different instruments. These approaches include 2D or 3D data fusion (14, 15) or multimodal characterization (16), where multiple data sets are collected and registered resulting in multilayered or multidimensional data at high resolution. Another example is the use of the

digital twin approach (14, 17), which links an experimentally measured structure or microstructure to a virtual representation of the same structure or microstructure. These new approaches integrate information across length and time scales (18). They also generate large multimodal and multidimensional data sets that are complex to analyze and therefore drive the use of advanced data and image processing and analysis, including machine learning and computer vision approaches.

The emerging tools described here capture the heterogeneity of deformation associated with microstructure and slip localization and provide guidance for the development of new models for microstructure–mechanical property relationships. Slip localization occurs with nonuniform motion of dislocations at the scale of individual or small groups of grains and is observed to strongly influence mechanical properties such as fatigue strength, yield strength, hardening, and ductility (19–21). For instance, fatigue crack nucleation and early propagation in metallic materials originate from intense, irreversible slip localization that develops within selected grains of a microstructure at the earliest stages of deformation (19). Another example is texture-induced modification of the connectivity of the slip localization events that result in a change in the macroscopic yield strength (20). This review details new insights on slip localization and its effect on macroscopic properties, gained by the use of innovative experimental and numerical tools.

2. PROBING BULK RESPONSE WITH HIGH-RESOLUTION MEASUREMENTS OVER LARGE FIELDS OF VIEW

In Section 2.1, some of the innovative imaging and diffraction techniques used to capture the relationship between microstructure and slip localization in metallic materials are introduced. These emerging techniques provide unique opportunities to capture the effect of metallic materials' 2D or 3D microstructures, chemical compositions, and crystal structures by statistical, representative, and/or correlative measurements. These techniques are used to capture the characteristics of slip within individual crystallographic grains over large fields of view, and they highlight the importance of the multiple length scales over which heterogeneous slip processes occur and thus exert a strong influence on macroscopic mechanical properties.

2.1. Quantification of Slip Localization by High-Resolution Digital Image Correlation

Over the past two decades, HR-DIC in the SEM has emerged as an important tool for quantitatively capturing deformation processes at the nanometer scale over large fields of view such that the effects of microstructure heterogeneities and the distribution and characteristics of deformation can be elucidated (22). Tatschl et al. (1) demonstrated the ability to capture high-resolution deformation fields by combining optical imaging DIC methods with the SEM for enhanced resolution. Subsequently, efforts to increase the resolution of the technique have led to refinement of the speckle patterning method (23–25) and SEM imaging parameter optimization to minimize spatial and/or drift distortions and to reduce beam scanning defects (25–27). The resulting increases in spatial resolution and strain sensitivity permit the imaging of direct signatures of single deformation processes during plastic deformation, such as slip (2, 22, 28–39), deformation twinning (40, 41), or grain boundary sliding (42). With the development of SEM image acquisition automation and automated strain field stitching procedures (38, 41, 43), these localization events are obtained over millimeter-scaled regions, making HR-DIC measurements statistically relevant at the microstructural scale of most polycrystalline engineering alloys (2, 19, 41). In addition, complex loading conditions such as cyclic, biaxial, or high-temperature loading (36, 44) have been applied, with HR-DIC measurements still able to be performed. The HR-DIC technique has also

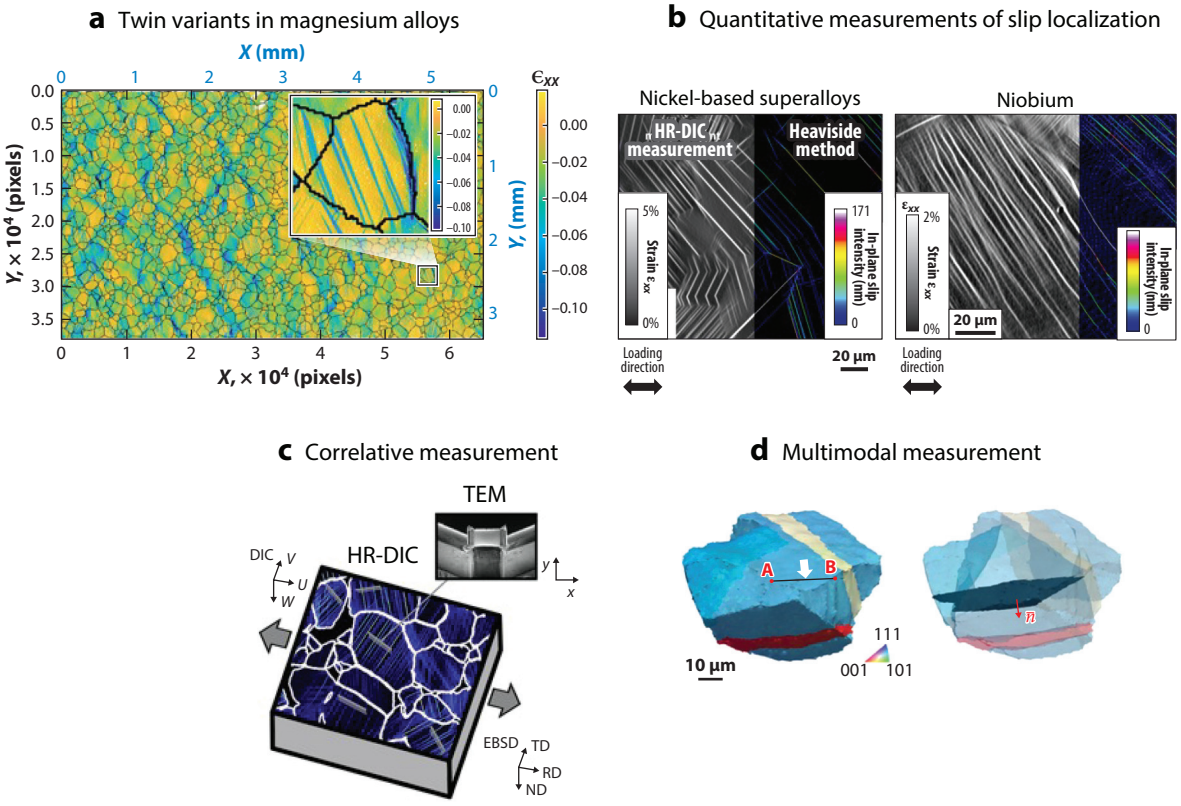

Figure 1

Representative quantitative and correlative measurements of deformation events by HR-DIC. (*a*) HR-DIC measurement over a large field of view in a magnesium alloy allowing twin variant identification. Panel adapted from Reference 41 with permission from Springer Nature. (*b*) Quantitative measurement of deformation slips by the Heaviside-DIC method in (*left*) a nickel-based superalloy and (*right*) a niobium alloy. The intensity of each slip event that developed during deformation is provided in nanometers. Panel adapted from Reference 19 with permission from AAAS. (*c*) Correlative measurement between HR-DIC, EBSD, and TEM to identify dislocation activity that led to slip localization in a titanium alloy. Panel adapted from Reference 31 with permission from Elsevier. (*d*) Multimodal data between HR-DIC and 3D grain structure measurements merged to capture the subsurface grain structure effect on surface slip activity. Panel adapted from Reference 46 with permission from Elsevier. Abbreviations: EBSD, electron backscatter diffraction; HR-DIC, high-resolution digital image correlation; ND, normal direction; RD, rolling direction; TD, transverse direction; TEM, transmission electron microscopy.

recently been adapted for data fusion between correlative multimodal measurements (31, 45–48), dynamic measurements (38), and quantitative measurements (33, 49).

HR-DIC measurements performed over 10 mm^2 during deformation of a magnesium alloy (shown in **Figure 1*a***) allowed a statistical analysis of the deformation twin variants that form relative to the grain structure (40, 41). A similar study related slip localization to microstructure for a number of materials including titanium, nickel-based superalloys, stainless steels, aluminum, niobium, high-entropy alloys, and alloys processed by additive manufacturing (19). Slip localization measurements by HR-DIC enable identification of operative slip systems (31, 50), slip intensity (49), slip length, and slip morphology (19). The resolution of HR-DIC was further enhanced by treating the deformation induced by slip as discrete discontinuities rather than averaging the deformation across the slip bands using a continuum-type approach. The development of these

advanced discontinuity codes (49, 51–54) enabled quantitative measurements of localized slip-induced displacements (see **Figure 1*b*** for a nickel-based superalloy and a niobium alloy after plastic deformation). Each slip event and its intensity, given in nanometers, are captured over square-millimeter fields of view, revealing the microstructure features that induce intense slip localization. HR-DIC measurements have also been integrated with transmission electron microscopy (TEM) (31) or 3D grain measurements (TriBeam tomography 3D EBSD or synchrotron X-ray near-field grain mapping) (45, 46, 55) to provide correlative and multimodal data sets that inform the role of the 3D grain structure on surface plastic activity. Using the combination of site-specific TEM and large field of view HR-DIC measurements in a titanium alloy (**Figure 1*c***), the active slip systems and dislocation activity were captured (31) to understand the details of the dislocation mechanisms that lead to slip localization. The combination of 3D grain structure and HR-DIC measurements to generate a 3D multimodal data set (**Figure 1*d***) extends plasticity observations by HR-DIC beyond surface-only measurements to the first subsurface layer of deforming grains. In addition, HR-DIC data measurements can facilitate the verification of numerical simulations such as crystal plasticity (CP) simulations (56), accelerating the identification of microstructure–mechanical behavior relationships.

Incipient plasticity in nickel-based superalloys (11) and titanium alloys (28) was observed by rarely occurring intense slip localization events at stresses far below the macroscopic yield strength. In a titanium alloy loaded to 65% of the yield strength, only two slip localization events were detected in more than 20,000 grains (**Figure 2*a***). Fatigue crack nucleation has been observed at these rare features due to the continued increase in slip amplitude during repeated cycling to the high-cycle fatigue regime in nickel-based superalloys (57) and titanium alloys (28). Interestingly, for all of the investigated titanium and nickel-based alloys, the majority of the incipient slip localization events and associated crack nucleation sites were observed near or at special boundaries (twin or twist boundaries) where slip developed parallel to the boundaries. Such a configuration is referred to as parallel slip configuration (33) and is the preferred mechanism for incipient slip localization and crack nucleation in various engineering alloys with face-centered-cubic (fcc) structures (19).

In fatigue, the amplitude of the most intense slip localization was observed to correlate with the fatigue ratio (fatigue strength divided by yield strength) for a variety of metallic materials (19). The well-known relationship between the yield strength and fatigue ratio is followed on the left side of **Figure 2*b***, with high-yield strength materials displaying low fatigue ratios. The data on the right side of **Figure 2*b*** result from a statistical and quantitative investigation of slip localization during the first fatigue cycle for over 10,000 localization events. The slip length normalizes the data to include the grain size effect. Several fundamental aspects of the fatigue behavior were demonstrated: (*a*) Materials that develop high and irreversible slip localization have low fatigue ratios; (*b*) body-centered-cubic (bcc) materials generally show a much more homogeneous distribution of plasticity that manifests itself in a high density of localization events with low intensity, resulting in a high fatigue ratio; and, most importantly, (*c*) the slip localization state after the first cycle controls the fatigue strength of metallic alloys.

HR-DIC measurements also provided insight into the contribution of slip localization to the overall plastic deformation. Slip localization was observed to contribute to more than 90% of the overall plastic deformation at low macroscopic plastic deformation levels in nickel-based superalloys (58), while other forms of nonlocalized plasticity such as geometrically necessary dislocations (GNDs) contributed more significantly at higher levels of deformation. This highlights the importance of slip localization at low levels of plastic deformation.

Another insight provided by the statistical investigation of slip localization is how slip localization events are connected through the microstructure in metallic materials. For instance, regions

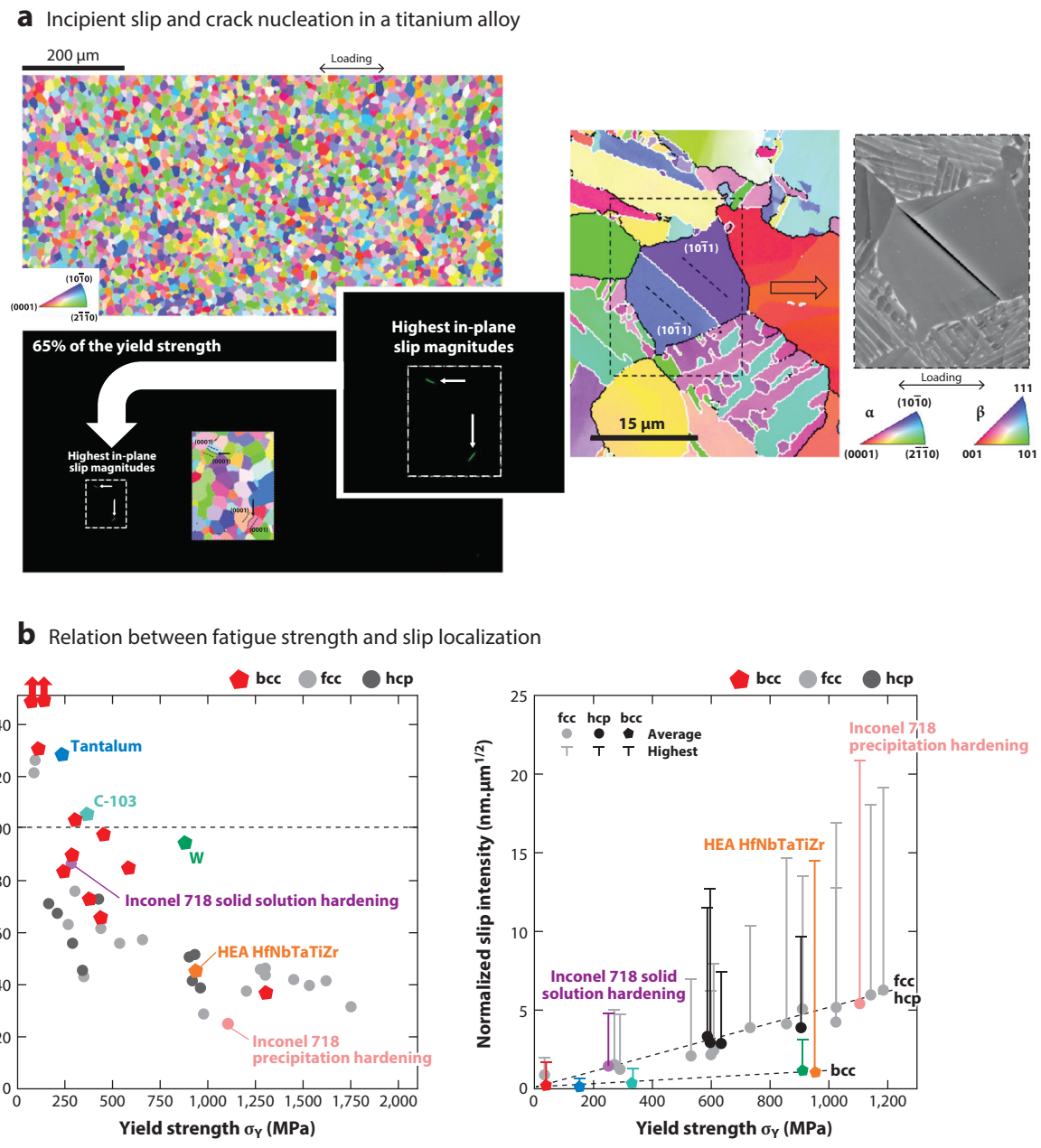

Figure 2

(*a*) Incipient slip localization in a titanium alloy loaded at 65% of its yield strength. Only two slip events are observed along twist boundaries over the 2-mm^2 investigated region. Fatigue crack nucleation is also observed at twist boundaries in the investigated titanium alloy. Panel adapted from Reference 28 with permission from Elsevier. (*b*) Relationship between fatigue strength and slip localization in metallic materials with bcc, fcc, and hcp crystal structures. The fatigue ratio (*left*) is observed to be correlated with the intensity of the highest slip localization event after the first fatigue cycle (*right*). The dots and bars correspond to the average and highest intensity of all detected slip localization events, respectively. Panel adapted from Reference 19 with permission from AAAS. Abbreviations: bcc, body-centered cubic; fcc, face-centered cubic; hcp, hexagonal close-packed; HEA, high-entropy alloy.

of grains with low misorientation, such as microtextured regions in titanium alloys, promote the connectivity of slip events and consequently reduce the yield strength (59, 60). These previously described observations demonstrate the necessity of investigating the characteristics of slip such as the slip intensity, slip connectivity, and slip irreversibility to inform the relationship between microstructure and mechanical properties.

2.2. Electron Channeling Contrast Imaging

Electron channeling contrast imaging (ECCI) enables characterization of dislocations in bulk samples in the SEM environment rather than, for instance, in thin foils in a TEM environment. A detailed discussion of the history of the use and development of ECCI and EBSD is given in a review article by Wilkinson & Hirsch (61). ECCI is a particularly useful method for quickly determining dislocation densities and spatial distributions over large fields of view (62) since it requires only a backscattered electron (BSE) detector in the SEM and can be performed on bulk material, potentially eliminating the need for TEM observations. It also provides a unique opportunity for the direct observation of dislocation glide, as shown in Reference 63. With improvements in SEM imaging automation and image analysis algorithms, ECCI measurements are emerging as a tool for defect (see **Figure 3*a***) and small-scale microstructure characterization at the nanometer scale over large fields of view (62, 64).

In metallic materials, ECCI provides unique opportunities to elucidate the relationships between mechanical behavior and plasticity (65, 66). ECCI resolves some of the confounding issues associated with in situ TEM studies, including the requirement of a thin foil, preventing thin-foil imaging effects, the small and not necessarily representative regions that are able to be studied

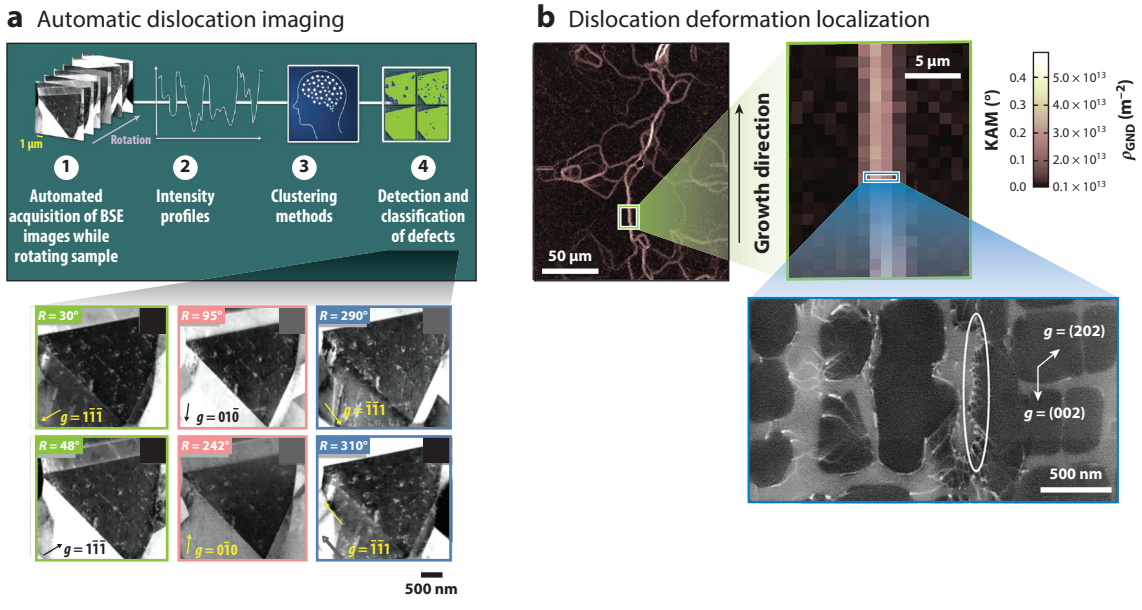

Figure 3

Automated and correlative measurement of defects by ECCI. (*a*) Methodology for quantitative and automatic dislocation characterization of a bulk sample in a scanning electron microscope. Panel adapted from Reference 62 with permission from Elsevier. (*b*) Dislocation arrangements in the bulk of a specimen spatially determined via correlation between electron backscatter diffraction and ECCI measurements. Panel adapted from Reference 67 with permission from Elsevier. Abbreviations: BSE, backscattered electron; ECCI, electron channeling contrast imaging; GND, geometrically necessary dislocation; KAM, kernel average misorientation.

with TEM, and the straightforward specimen preparation for ECCI. The efficacy of ECCI for capturing plastic deformation has been broadly demonstrated including the systematic study of localization during creep deformation in single crystal Ni-based superalloys (67), shown in **Figure 3*b***. ECCI has also been used to reveal the strain-hardening behavior of twinning-induced plasticity steels (64), dislocation structures leading to slip localization in iron and 304L stainless steel deformed by fatigue (68) and dislocation cells, veins, and persistent slip in Cu and stainless steels (69, 70). Additionally, recent studies show the dislocation structures that develop in Cu during fatigue with increasing strain amplitudes (71) and the effects of phase fraction on deformation behavior in a dual-phase high-entropy alloy (72), and comparisons have been made between model predictions of dislocation structures and direct ECCI observations in 316L steel (73).

2.3. Transmission Scanning Electron Microscopy

The recent availability of solid-state scanning transmission electron microscopy (STEM) detectors for SEMs with high-quality field emission sources allows for the direct imaging of dislocations over volumes much larger than those available in TEM (74). Combined with innovative micromechanical stages and with increased versatility for in situ measurements due to relaxed vacuum chamber constraints, the dynamics of dislocation motion and strain localization can be directly observed (75, 76) (**Figure 4**). In this approach, referred to as TSEM, imaging can be conducted in bright-field, dark-field, and weak-beam modes. The combination of a lower extinction distance, lower accelerating voltages in the SEM compared with those in TEM, and a reduction of dynamical scattering due to bend contours and thickness fringes results in sharper dislocation contrast (74). Additionally, STEM imaging has improved signal-to-noise ratio compared with conventional TEM imaging due to the convergence of the beam (77). As there are no postspecimen lenses, the camera length used in imaging is constrained; however, with the large SEM chamber,

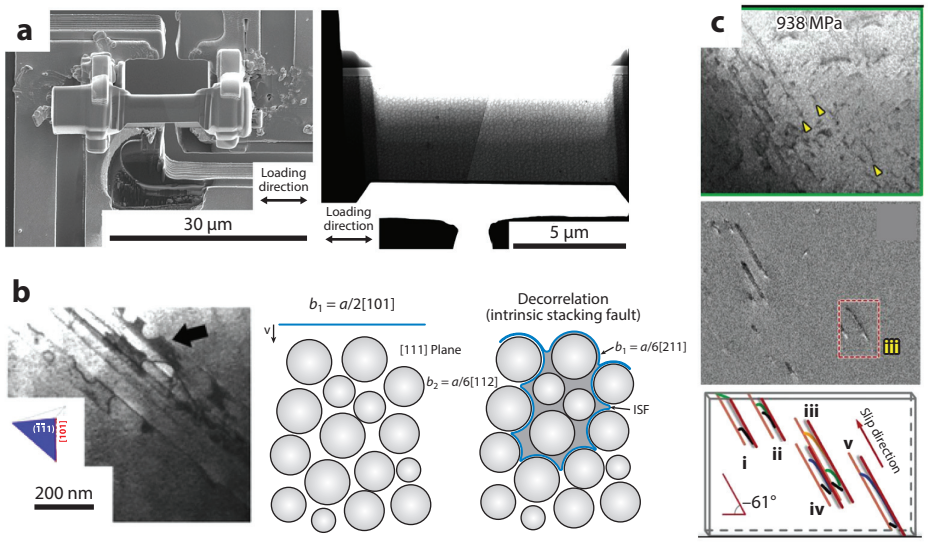

Figure 4

Dislocation dynamics leading to slip localization. (*a*) Use of transmission scanning electron microscopy to facilitate in situ testing with transmission imaging. Panel adapted from Reference 76 with permission from Elsevier. (*b*) Dislocation dynamics in a nickel-based superalloy. Panel adapted from Reference 76 with permission from Elsevier. (*c*) Edge and screw dislocation components in a high-entropy alloy. Panel adapted from Reference 78 with permission from AAAS.

additional detectors such as EBSD, energy dispersive X-ray spectroscopy, BSE, secondary electron, and cathodoluminescence TSEM can provide a wealth of multimodal information.

Figure 4 shows examples of TSEM imaging of dislocations gliding along slip planes in a nickel-based superalloy and a refractory multiprincipal element alloy (MPE) (76, 78). In the polycrystalline nickel-based alloy (76), TSEM reveals a complex strain localization process, whereby partial dislocations initially residing in the fcc matrix are pushed into the ordered $L1_2$ precipitates, creating superlattice intrinsic stacking faults, sometimes across multiple precipitates. The localization process then proceeds as additional dislocations gliding on the same plane push trailing partials through the precipitates, completely erasing the stacking faults. This repeated faulting and defaulting process disrupts the shape of the coherent precipitates on the plane of localization, softening the material locally. The benefits of the dynamical aspects of the TSEM approach are also leveraged during in situ straining of a bcc MoNbTi MPE alloy (78), where gliding dislocations show significant nonscrew character unlike their conventional refractory element counterparts that are dominated by the glide of screw dislocations. Similarly, under cyclic loading, an HfNbTaTiZr MPE alloy displays a distinctly different localization behavior compared with conventional bcc alloys, suggesting that intrinsically different behaviors are possible when no single element dominates the compositional landscape (19).

2.4. Electron Backscatter Diffraction

Increases in EBSD collection rates and high-quality and high-resolution patterns have been enabled by the development of monolithic active pixel sensors (MAPS) and other direct electron detectors (79–83). Several research topics that will benefit from the continued development of faster, higher-quality EBSD detectors are (*a*) rapid high-quality data collection due to the fast readout and sparse sampling, (*b*) more rapid collection of high-angular-resolution EBSD (HR-EBSD) data, (*c*) higher-spatial-resolution EBSD data at lower accelerating voltage, and (*d*) more efficient application to a broader spectrum of materials classes. As shown in **Figure 5*a***, sparse sampling can be used to read out a limited number of pixel rows, which are sufficient for EBSD indexation, resulting in a significant increase in data collection speed (79, 80).

In serial sectioning experiments for 3D data collection, one of the most time-intensive steps is the EBSD data collection at each slice. An increase in data collection speed or quality can significantly reduce the time and cost of collection of a data set (84, 85). EBSD serial sectioning experiments have now become a robust technique for 3D microstructure characterization (86) that is widely used to identify microstructure–mechanical behavior relationships. With the development of software infrastructure, slicing, and cleanup approaches, 3D data sets such as those shown in **Figure 5*b*** can be rapidly generated to capture microstructure at the cubic millimeter–scale while having a submicrometer spatial resolution to capture grain shape, twins, and grain boundary networks. Furthermore, rich information beyond the crystallographic orientation is present in the diffraction patterns obtained by EBSD measurements. Integrated forward modeling approaches of electron diffraction use Kikuchi band sharpness (87, 88) to determine statistically stored dislocation densities, as shown in **Figure 5*c***, which can be combined with existing approaches to calculate GND densities (89–91). In parallel, the use of lower accelerating voltages enables researchers to collect data with a smaller interaction volume (87, 92), allowing collection from materials with small grain sizes (93), small features, and multiple phases that have typically necessitated TEM (94) or transmission Kikuchi diffraction (95), as well as materials with significant amounts of misorientation, whether from damage (96, 97), processing (98, 99), or inherent microstructure (85). The enhanced electron detection efficiency and the ability to operate at lower accelerating voltages also present opportunities for beam-sensitive materials and those that are prone to sample charging.

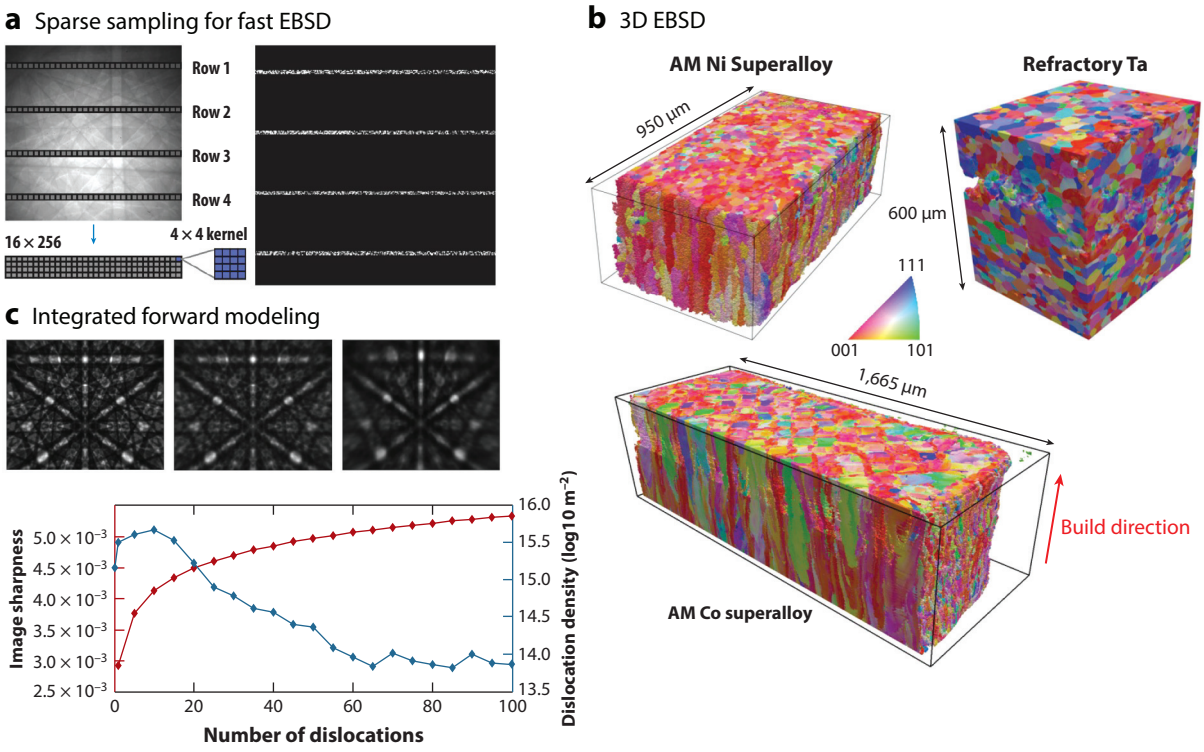

Figure 5

Sparse sampling, integrated forward modeling approaches, and 3D tomography using EBSD. (*a*) Sparse sampling is used on a MAPS direct electron detecting EBSD detector to decrease acquisition time. Panel adapted from Reference 80 with permission from Elsevier. (*b*) A 3D EBSD data set obtained using Tribeam tomography. Panel adapted from Reference 86 with permission from Elsevier. (*c*) An integrated forward modeling approach to determine the dislocation density based on Kikuchi band sharpness. Panel adapted from Reference 87 with permission from Elsevier. Abbreviations: AM, additively manufactured; EBSD, electron backscatter diffraction; MAPS, monolithic active pixel sensor.

The ability to generate and analyze 3D EBSD data has revolutionized the understanding of the role of rare microstructural features and characteristic microstructural neighborhoods in plastic deformation processes. For instance, combining slip localization measurements, numerical simulations, and 3D EBSD measurements, a governing effect of particular bulk triple junction lines on surface plasticity, crack initiation, and therefore material failure has been identified (46). Observations have shown that the full 3D microstructural neighborhood plays an important role in the development of plasticity and have indicated that conventional surface measurements are limited in their potential for determining the influence of microstructure without subsurface information. The contribution of this research is detailed in Section 3. In addition, 3D EBSD has revealed which 3D microstructural features promote damage initiation and propagation in superalloys (100), where the importance of the 3D subsurface grain boundary network and twin relations in predicting surface crack initiation in nickel-based superalloys was observed. Furthermore, 3D measurements validated the coherency of twins with slip planes in these fcc superalloys, enabling the application of crack initiation criteria (101) to large-area 2D measurements to determine the location of early strain localization, which leads to crack initiation (102).

Signatures of slip localization in metals can now be identified due to increases in EBSD angular measurement resolution. For instance, the changes in orientation within a grain can be determined

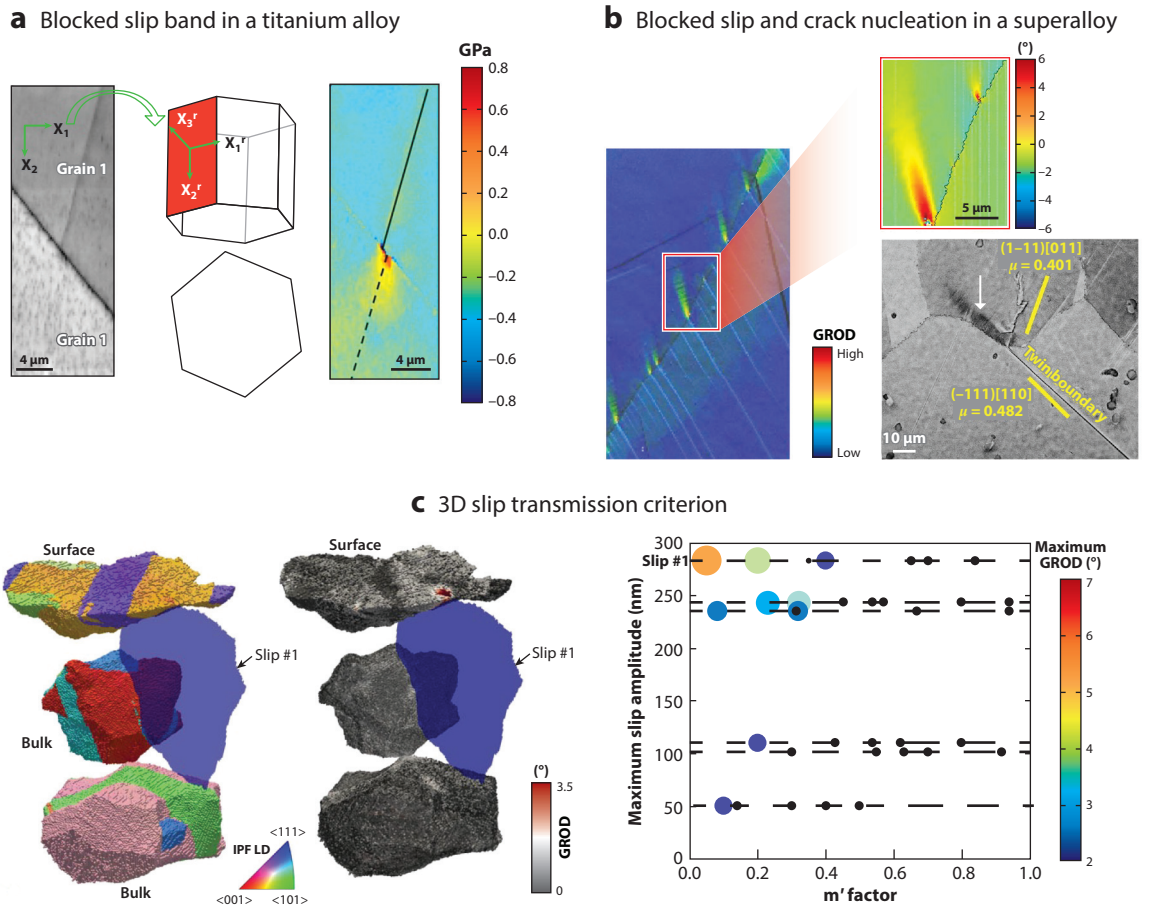

Figure 6

Blocked slip bands in titanium and nickel-based superalloys. (*a*) HR-EBSD of a blocked slip band at a grain boundary intersection, producing a localized stress concentration in the adjacent grain in a titanium alloy. Panel adapted from Reference 108 with permission from Elsevier. (*b*) HR-EBSD of blocked slip bands similar to those in panel *a* but in a superalloy and resulting in a crack nucleation event. Color images adapted from Reference 105 with permission from Wiley. Grayscale scanning electron microscopy image adapted from Reference 106 with permission from Elsevier. (*c*) 3D EBSD data set obtained from Tribeam tomography indicating intense lattice rotation due to the presence of a slip localization event. This intense lattice localization occurs when slip transmission of intense slip bands is prevented (low m′ factor). Abbreviations: EBSD, electron backscatter diffraction; GROD, grain reference orientation deviation; HR-EBSD, high-angular-resolution EBSD; IPF, inverse pole figure; LD, loading direction.

with higher resolution by measuring the shifts of subregions in electron backscatter patterns using cross-correlation techniques (103). The HR-EBSD technique has been used extensively to determine the GND content (91) and elastic strains (104). Interestingly, in titanium and nickel-based superalloys, slip localization is observed to produce intense stress concentration and lattice rotation in front of the slip band–grain boundary intersection as shown in **Figure 6*a*,*b***. These small-scale regions of high stresses and lattice rotation, referred to as microvolumes (105, 106), are important features that promote crack nucleation in nickel-based superalloys. These microvolumes were observed to develop at the surface and in the bulk of the specimen (55) and occur when slip transmission is prevented (low m′ factor) and slip localization is intense (**Figure 6*c***). It

has also been demonstrated that these slip band–induced stress fields can affect the deformation behavior even at the grain interior in bcc steel (107).

2.5. Bulk Measurement by Topotomography and Dark-Field X-Ray Microscopy

The penetrating power of hard X-rays has been used for decades to gather information from the bulk of deformed materials. X-ray topography, initially based on laboratory X-ray sources and photographic films or nuclear plates, provided projection images of dislocations and other crystal defects for more than 70 years (for a recent review, see Reference 109). With the constant increase in spatial resolution [thanks in particular to synchrotron light source upgrades (110)] and advances in detector technology, it is now possible to directly image plastic deformation events throughout the interior of cubic millimeter–scaled samples. X-ray TT combines the orientation contrast obtained in topography mode (109), where crystal defects locally alter the Bragg condition (resulting in contrast on the collected image), with tomography acquisition via the rotation of the crystal around the chosen scattering vector (111).

This technique can also be used with extended plate geometry if the scattering vector is normal to the plate in a variant termed diffraction laminography. This has been used to study slip localization in silicon and was able to map dislocation arrays in three dimensions with great accuracy (112). However, this use case is quite restrictive and may not be used other than in selected, well-oriented monocrystals.

The combination of X-ray diffraction contrast tomography (DCT) and TT was first used to image slip events with a polycrystalline Al–Li alloy (**Figure 7*a***) during in situ deformation and then relate these events to the 3D grain structure (8). Striking band contrast observed on the topographs could be related to individual slip systems activated and forming slip bands in the bulk of the material. Aside from analyzing the individual topographs, collected X-ray TT data can be further used to reconstruct the 3D orientation field within the crystal (right side of **Figure 7*a***). The reconstruction can combine data from several reflections and from X-ray DCT and TT (113) to improve the spatial resolution.

Thanks to progress in automation, a recent study using the X-ray TT technique in a titanium Ti-7Al alloy could more systematically map entire grain neighborhoods and therefore provide a statistical study of slip localization and transmission to the next grain, in grains located both at the surface and within the bulk (**Figure 7*b***). For surface grains, a comparison with HR-DIC measurements concluded that X-ray TT is able to capture slip bands exceeding a minimum shear amplitude of 50 nm. Furthermore, the study highlighted important differences between surface and bulk slip transmission regarding the transmission of plasticity to neighboring grains (9). In particular, it was shown that the often-observed network of continuous bands across different grains at the surface does not occur in the bulk, suggesting a strong impact of the free surface on the slip system selection.

The spatial resolution of full-field X-ray diffraction imaging techniques such as X-ray DCT and TT or near-field high-energy X-ray diffraction microscopy (HEDM) is inherently limited by detector technology. The X-ray-to-visible-light conversion process in the deployed X-ray imaging detectors limits the ultimate spatial resolution to about 1 μm. Moreover, the simultaneous illumination of extended (3D) sample volumes gives rise to highly convoluted signals on the detector, challenging the quantitative analysis and (tomographic) reconstruction of local orientation and elastic strain of the crystal lattice.

To alleviate and overcome this limitation, another X-ray diffraction imaging method termed DFXM has been developed (116). With this method an X-ray objective lens is placed in the diffracted beam and used to produce a magnified image on a detector that can be placed several meters away from the sample, achieving spatial resolutions better than 100 nm in the detector plane.

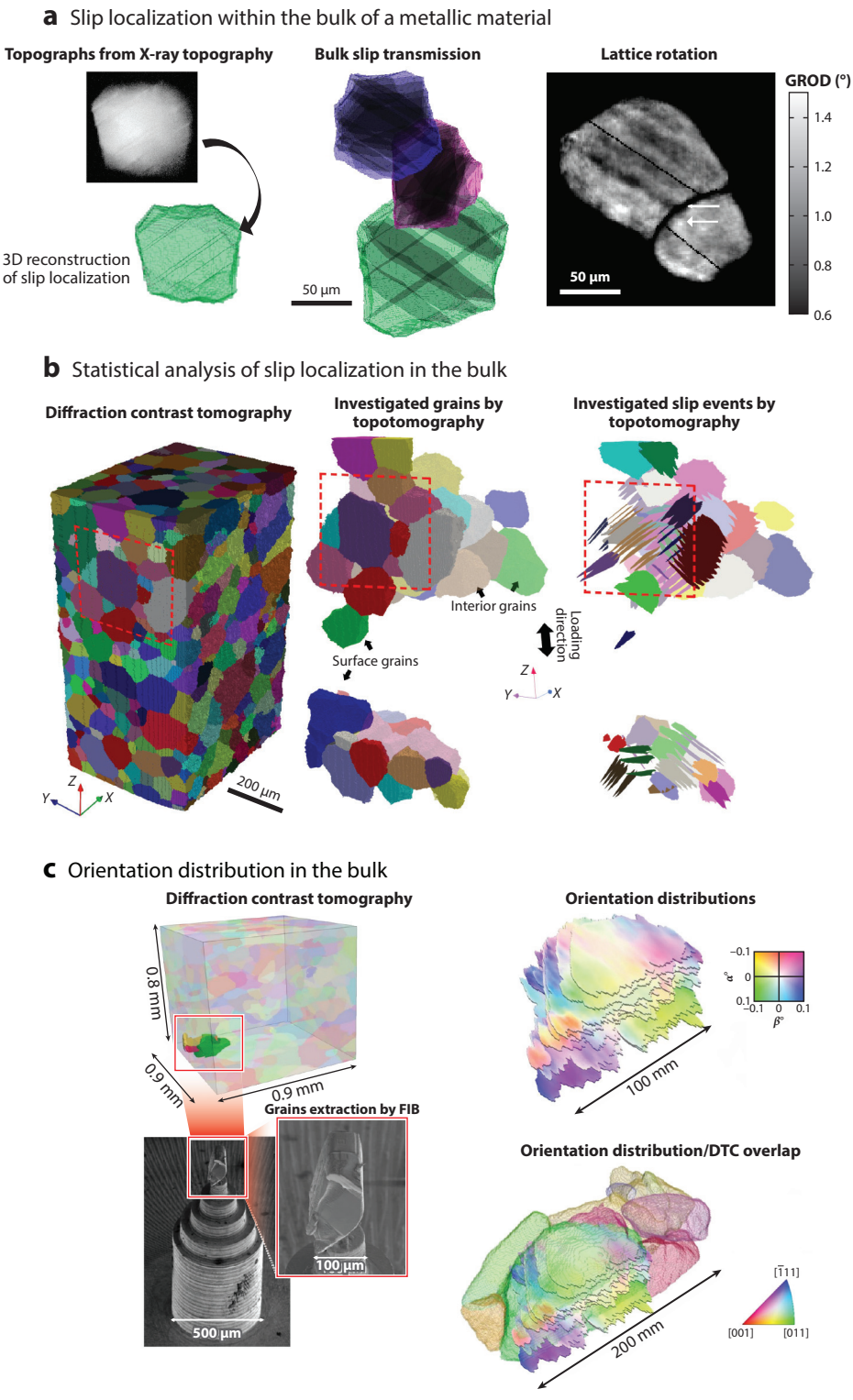

Figure 7

Bulk slip localization events probed by X-ray diffraction imaging methods. (*a*) Slip event identification in a deformed Al–Li alloy. Panel adapted from Reference 114 with permission from Elsevier. (*b*) Deformed titanium alloy Ti–7Al specimen studied using diffraction contrast tomography. Fifty-five grains were measured using topotomography to uncover the 3D network of activated slip planes. Panel adapted from Reference 9 with permission from Elsevier. (*c*) Dark-field X-ray microscopy experiment with a grain extracted from a fatigued nickel-based superalloy specimen. The $\alpha°$ and $\beta°$ indicate the orientation deviation along the principal axis. Panel adapted from Reference 115 with permission from Springer-Nature. Abbreviations: DTC, diffraction contrast tomography; FIB, focused ion beam; GROD, grain reference orientation deviation.

Focusing optics are used to produce a line beam (typically 1 μm thick) to illuminate a specific layer of the sample (either a monocrystal or a grain within a polycrystal), and 3D reconstructions can be achieved by stacking several layers. A series of tilt motors allows scanning of the sample and measuring of both local orientations (mosaicity scans) and strain fields (strain scans) within the bulk. In a typical DFXM experiment, only one reflection is usually captured, preventing the measure of all strain components.

DFXM has been used to visualize individual dislocations and their strain fields, such as in References 117 and 118. Porz et al. (119) were able to study a full dislocations array in a silicon crystal deformed by indentation. Yildirim et al. (120) studied a cold-rolled Fe–Si–Sn alloy that was heated in situ to trigger recrystallization and were able to capture the presence of shear bands in the as-deformed sample. Upon heating at 610°C, higher misorientation zones such as grain boundaries or deformation band junction points were found to be preferential nucleation regions. DFXM can also be used advantageously to magnify specific grains in a deformed sample of known microstructure (typically one that has already been characterized by X-ray DCT or HEDM). However, this may involve extracting a smaller region of interest in order to maintain sufficient transmission at the X-ray energies available at the current implementation of the instrument [at the European Synchrotron Radiation Facility (ESRF), beamline ID06] (121). Using this approach, Gustafson et al. (115) investigated the orientation and strain fields in a specific grain of a fatigued nickel-based superalloy specimen. The gauge section was first mapped using HEDM and then cyclically loaded to develop intragranular deformation localization due to plasticity. A specific location was extracted using focus ion beam milling and characterized via DFXM to access the local orientation and strain fields of the grain of interest (see **Figure 7*c***). This analysis demonstrated the occurrence of intense slip localization near a bulk twin boundary during fatigue of a nickel-based superalloy.

2.6. Polychromatic X-Ray Diffraction Microscopy and Scanning 3D X-Ray Diffraction

Similar to electron microscopy, scanning techniques deploying a focused X-ray probe have been developed over the past two decades. The ultimate spatial resolution is now given by the size of the X-ray probe and the positional stability and precision of the sample positioning system. Values reported from dedicated synchrotron endstations (122, 123) currently range between 100 and 500 nm. One has to further distinguish between polychromatic (Laue) microdiffraction and monochromatic beam variants, which imply sample rotations.

Polychromatic microdiffraction endstations such as 34-ID-E at the Advanced Photon Source (APS) or BM32 at the ESRF deploy achromatic, reflective focusing optics (124) and exploit X-ray energies in the range of 7–25 keV. A wire-scanning technique termed differential aperture X-ray microscopy (DAXM) (125) allows for isolating diffraction information from limited (submicrometer) sample subvolumes and hence the characterizing of 3D sample volumes by means of a 3D scanning procedure [one translational wire scan per sample (X, Y) position]. The tremendous increase in brilliance provided by the ongoing upgrade of all major synchrotron sources worldwide and the availability of fast-readout, highly efficient X-ray detector systems results in acquisition rates of several tens up to hundreds of hertz. From the collected and postprocessed Laue patterns, one can extract the local crystallographic orientation and deviatoric part of the elastic lattice strain tensor. The 34-ID-E endstation furthermore offers optional switching to monochromatic beam and energy scans, enabling accurate peak position and full width at half maximum (FWHM) analysis of the crystal reflection curve. Research by Li et al. (126) shows a cross-sectional view of a grain in a specimen of stainless steel that has undergone fatigue loading in the low-cycle regime. As shown in **Figure 8*a***, the presence of (persistent) slip bands is clearly visible in the FWHM map acquired in a monochromatic beam. Moreover, analysis of the local lattice orientation revealed a subdivision

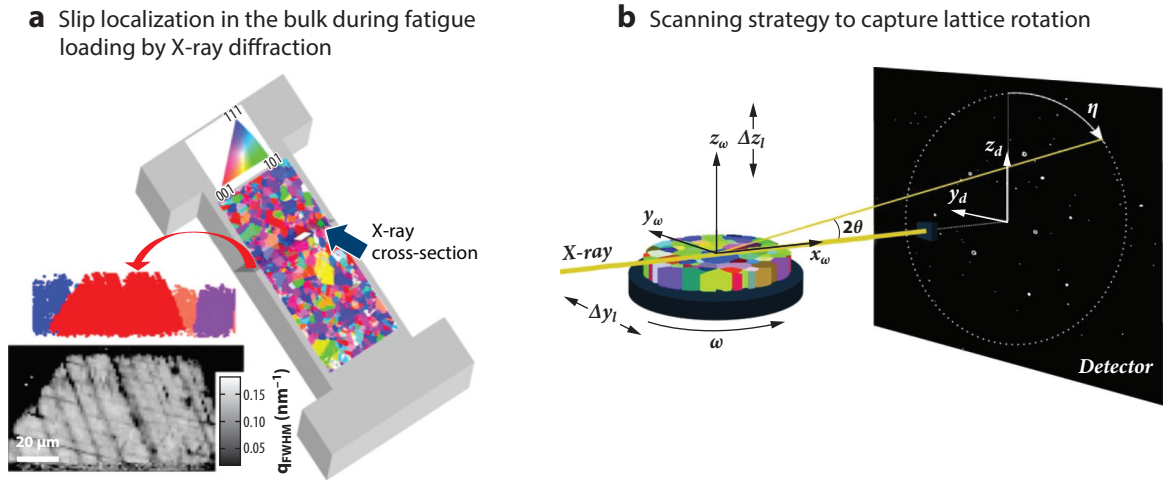

Figure 8

(*a*) Network of persistent slip bands in stainless steel as revealed by the monochromatic beam energy and wire-scanning method at 34-ID-E. Panel adapted from Reference 126 with permission from PNAS. (*b*) Principle of scanning 3D X-ray diffraction. Panel adapted from Reference 129 with permission from the International Union of Crystallography. Abbreviation: FWHM, full width at half maximum.

of the grain into weakly misoriented domains, separated by these bands. The analysis of lattice strain before and after an incremental plastic deformation of the same sample reveals the presence of high gradients in lattice strain at the intersection of the primary and secondary slip bands.

Whereas depth resolution (along the X-ray beam) in DAXM is achieved by the wire-scanning method (no sample rotation and no mathematical inversion involved), monochromatic beam scanning 3D X-ray diffraction (3DXRD) (127, 128) follows a different strategy: The sample rotation stage is translated in small steps in the direction perpendicular to the rotation axis while the sample is continuously rotated over 180° for each of these lateral positions (see **Figure 8*b***). This procedure is repeated for a series of vertical sample positions. Scanning 3DXRD can be used at higher X-ray energies and offers more space and flexibility for sample environments (mechanical load, temperature, etc.). Various analysis strategies can now be used to recover the local orientation and (full) elastic strain tensor from such sets of projection data (122, 129). The diffraction signals recorded for a given grain are integrated along the in-depth (beam) direction, and the solution of the inverse problem depends on the magnitude of the orientation and strain gradients inside the material. Henningsson & Hendriks (130) demonstrated successful recovery of the elastic strain components for the case of small intragranular orientation spread and report a strain sensitivity on the order of 10^{-4}. The solution of the more general problem (i.e., a combination of orientation and strain gradients) is actively being worked on, and the ultimate sensitivity is yet to be determined.

3. MULTIMODAL MEASUREMENTS AND CORRELATIVE TECHNIQUES

Even within the same instrument (e.g., SEM, TEM, AFM) there are many different imaging modalities (SE, BSE, EBSD, STEM) that reveal different information about a material. Spatial correlation of the different phases present, local grain orientation and lattice rotation, grain boundaries and other interfaces, defects, and inclusions are all important for understanding deformation. Since the measurements of, for example, slip activity and grain structure are not encoded

together into one single measurement method, these analyses inherently involve the collection of multiple data modalities. The signature of slip traces, extrusions formed onto the specimen's surface, can be detected using any technique sensitive to the surface topology. This includes secondary electron imaging, AFM, ECCI, optical microscopy (131), and DIC. On the other hand, crystal orientation data are generally collected by means of EBSD or X-ray grain mapping. These combined measurements are key to understanding the development of plastic localization as a function of the microstructure. From a theoretical standpoint, they enable an understanding of strain partitioning in multiphase materials (132) and can be used to extract critical resolved shear stresses (133) or derive slip transmission criteria. They also can calibrate CP (56, 134–136) and discrete dislocation dynamics (DDD) models (51).

Unlocked by recent developments in software, hardware, and instrumentation, data sets have been increasing tremendously in volume (137). State-of-the-art techniques are now able to probe slip localization with unmatched depth and precision including high-resolution maps, time-resolved or dynamic measurements (33), and 3D or 4D data (46). For example, an HR-DIC map may gather more than 10,000 × 10,000 pixels, collected over multi-millimetric fields of view with nanometer resolution in slip intensity, and an ECCI data set contains numerous high-resolution images resolving individual dislocations or slip bands. As a result, combined data sets are usually giga- to terabytes in size.

This newly accessible knowledge can directly inform microstructure optimization as well as alloy design strategies for stronger, fatigue-resistant, and damage-tolerant materials (138). However, the analysis of large data sets can become overwhelming if carried out manually. While smaller multimodal data sets are easily comprehended and can be manually aligned spatially, larger data sets encompassing hundreds to thousands of grains require automated and accurate data modality alignment. Tasks such as counting the number of slip bands per grain, identifying the active slip systems, or calculating the cumulative slip localization require some level of automation to fully scale to the sizes required for a statistical analysis representative of the grain population.

3.1. Accurate Alignment Strategies for Large Microstructure Areas or Volumes

Differences in beam scanning artifacts, beam drift, sample charging, geometrical scanning distortions, and sample or instrument misalignment will impact multimodal data collection with at least two different detectors. Indeed, each detector comes with its own artifacts and spatial and angular resolution, and the information contained in each pixel may come from interaction volumes that vary between the primary beam and the sample. This results in complex distortions, particularly when different dwell times, voltages, and tilt angles are used for each detector (139). In a SEM, EBSD is usually the most heavily distorted data modality due to the highly tilted sample during data collection. Modality alignment routines use various assumptions regarding the shape of the distortion function (affine, trapeze, barrel, polynomial) and the definition of point sets (e.g., fiducials, microstructural features, sample shape) visible in all detector modes and used to define this function (43, 140–147). Point-set definition and registration are particularly challenging due to differences in feature contrast and imaging resolution between modalities. Attempting to address this challenge, clustering (43, 148) and microstructure digitization routines are being used to preprocess the different data modalities. Currently, this step is generally performed after alignment and is a central part of automated data analysis.

3.2. Microstructure and Plastic Strain Field Digitization Frameworks

The purpose of digitization is to create a numerical rendering of the microstructure and features of plasticity, with the aim of studying eventual correlations and conducting statistical analyses. Amid

the variety of data modalities collected to probe either the plastic localization or the microstructure, no unified framework currently exists to analyze correlated data sets. Isolated efforts have led to the development of custom frameworks that build upon preexisting software for microstructure feature segmentation (9, 149), such as DREAM.3D (150), pymicro (151), or commercially available EBSD software. These are convenient tools to identify individual grains and boundaries, as well as their respective properties. Two approaches have been used to featurize the plastic strain field: segmentation using conventional image processing tools and computer vision. Using iterative Hough transformations and Bresenham's algorithm, Charpagne et al. (152) were able to vectorize thousands of slip bands in Ti-6Al-4V and Inconel 718 deformed at room temperature. It is worth noting that all slip bands exhibited a planar character, an essential aspect incorporated into the workflow. Clustering techniques overcome this obstacle by allowing minimal assumptions on the shape of the objects of interest. The research efforts of Daly and colleagues have led to the successful identification of both slip bands (43) and deformation twins (40) in correlated DIC-EBSD data sets, which has allowed for the identification of the active twinning systems without conventional trace analyses.

3.3. New Insights from Slip Trace Analysis

Slip trace analyses have been carried out manually for decades to identify key mechanisms of plastic localization and slip transmission (153–157), generally with the goal of determining the active slip or twinning system. In large data sets, manual analysis of thousands of slip traces is obviously impractical. When a slip trace is visible, automated assessment of the active slip plane consists of computing the candidate traces from potentially active systems and comparing them with the experimental trace using a deviation tolerance. This tolerance should depend on the lattice structure (number of candidate traces). When several slip directions are active onto the plane, most researchers will follow the assumption that the one with the highest Schmid factor is active, which is one limitation of the sole analysis of the trace. To increase the confidence of the slip system determination, Chen & Daly (50) have proposed a complementary metric, the relative displacement ratio (RDR), calculated from HR-DIC data. When added to the Schmid factor as a constraint, the RDR has proven particularly successful at identifying slip systems in several hexagonal-close-packed (hcp) materials (31) (**Figure 9*a***).

New techniques such as Heaviside-DIC offer the opportunity to identify both the slip plane and direction on the basis of the analysis of the discontinuity when the crystal orientation is known (49). Charpagne et al. (140) have automated the procedure, leading to the identification of over 80% of the active slip systems in an fcc superalloy in an automated manner (**Figure 9*b***). However, classic slip trace analysis, either manual or automatic, is of limited use when the slip band morphology is wavy or when bands appear locally discontinuous as a result of diffuse slip or extensive cross-slip. Alternative postprocessing routines relying on the collection of correlated SEM-DIC and EBSD data are currently emerging in efforts by Hoefnagels and colleagues (158) (**Figure 9*c***). They are an attractive alternative in the presence of complex slip activity and particularly relevant in the case of materials with hcp or bcc lattices or fcc materials deformed at high temperature.

3.4. Correlative Analyses to Bridge Length Scales and Dimensions

With the advent of nanoscale DIC (34) and 3D characterization techniques, correlative analyses bridge length scales and bring a 3D perspective to 2D measurements collected on free surfaces. Vermeij et al. (35) have recently designed a correlative nanomechanical testing framework that allows the collection of DIC, BSE, and EBSD data on the front and rear sides of specimens

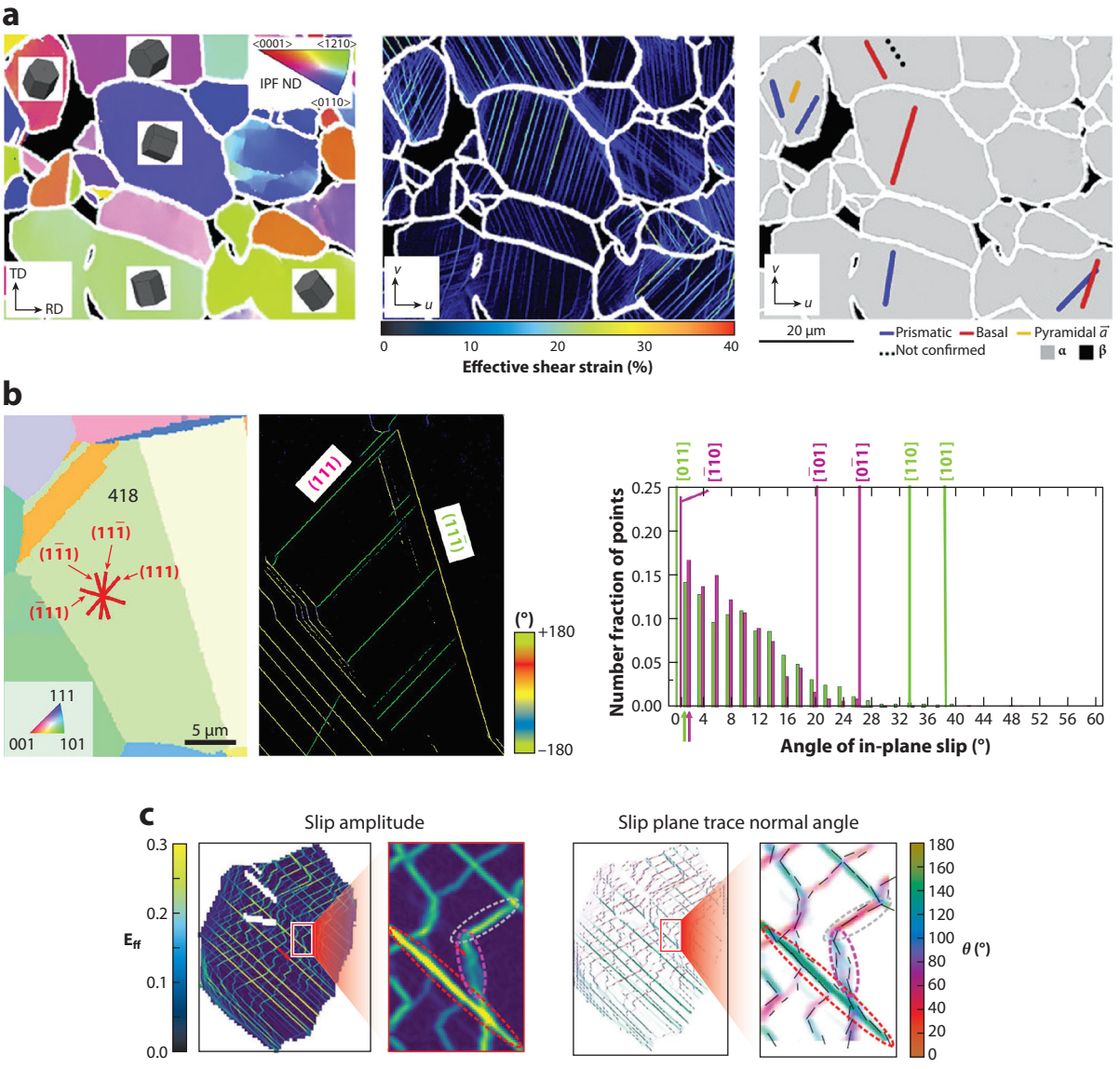

Figure 9

Automated slip trace analyses from coupled DIC-EBSD data sets. (*a*) Coupled Schmid factor and RDR approaches in hcp titanium. Panel adapted from Reference 31 (CC BY 4.0). (*b*) Slip trace and direction determination from Heaviside-DIC/EBSD data sets. Panel adapted from Reference 152 with permission from Elsevier. (*c*) Cross-slip identification in the fcc nickel-based alloy RR1000 after 0.02% macroscopic strain, showing the slip system amplitude field and the angle between the horizontal direction and the slip plane orientation, with transparency inversely scaled with the slip amplitude. The red ellipses highlight areas where cross-slip occurs. Panel adapted from Reference 158 (CC BY 4.0). Abbreviations: bcc, body-centered cubic; DIC, digital image correlations; EBSD, electron backscatter diffraction; hcp, hexagonal-close-packed; HR-DIC, high-resolution DIC; IPF, inverse pole figure; ND, normal direction; RD, rolling direction; RDR, relative displacement ratio; TD, transverse direction.

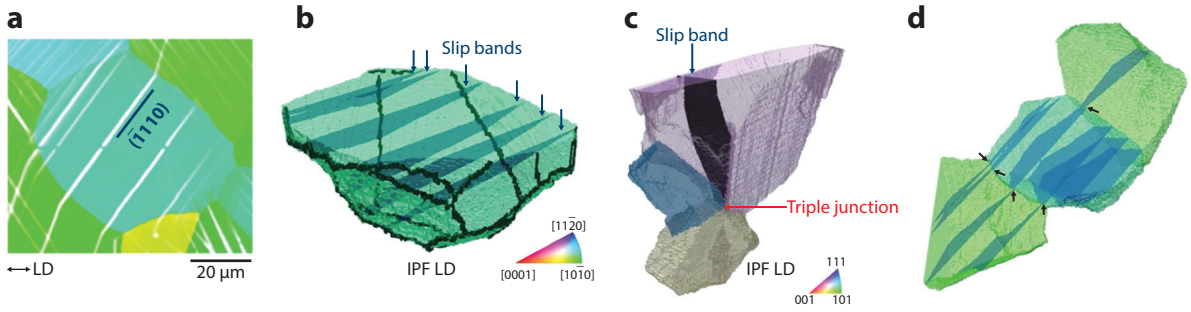

Figure 10

3D visualization of slip bands from HR-DIC/3D EBSD correlated data sets. (*a*) 2D slip traces visible on the surface of the 3D EBSD data set and identified slip plane. (*b*) Slip trace projected into the 3D microstructure. (*c*) Slip band emerging from a triple junction in a nickel-based Inconel 718 superalloy. (*d*) Long-range transmission in Ti-7Al shown spanning across three grains. Figure adapted from Reference 45 with permission from Springer Nature. Abbreviations: EBSD, electron backscatter diffraction; HR-DIC, high-resolution digital image correlation; IPF, inverse pole figure; LD, loading direction.

with carefully designed geometry, followed by a microstructure-to-strain alignment procedure to couple the different data modalities. Using this framework, the authors were able to link nanoscale and mesoscale deformation processes in the martensite and ferrite phases in steel samples and relate incipient plasticity to cracking phenomena in intricate microstructures. The collection of DIC data on the front and rear sides of a thin specimen also allows for the extrapolation of the subsurface to 3D behavior.

Indeed, as the traces observed on a specimen's surface are the result of bulk processes, investigation of slip traces in three dimensions gives new perspectives on the origins of slip band formation as a function of the complete, 3D microstructure. Charpagne et al. (159) have led these efforts and proposed the first 2D-to-3D multimodal data merging framework that reconstructs slip bands in 3D EBSD data sets using 2D slip traces (45). Using these analyses, they were able to reconstruct over 1,000 slip bands in 3D EBSD data sets measuring over 500 μm × 500 μm × 500 μm in both Inconel 718 and Ti-7Al after deformation beneath and beyond the macroscopic yield point. The procedure consists of projecting automatically identified slip planes associated with each slip trace into the 3D microstructure, as shown in **Figure 10*a*,*b***. Statistics depicting how the slip bands relate to the subsurface microstructure features are extracted from these rich data sets. As such, Charpagne et al. (159) have highlighted the role of triple junctions (3D lines joining three individual grains) for slip band formation, as illustrated in **Figure 10*c***. Furthermore, while this technique reconstructs slip bands in only the first layer of grains, it still reveals possible surface effects. In a highly textured Ti-7Al data set, the authors observed long-range slip transmission, revealing its prominent role in the development of the plastic localization network (**Figure 10*d***). All transmitted slip bands appeared to be connected via a point located on the free surface, suggesting possible surface effects on the slip transmission behavior, as discussed in Section 2.5.

The experimental techniques and approaches presented in Sections 2 and 3 take advantage of recent improvements in detector technology, hardware, and software to collect high-resolution data over large fields of view. Furthermore, these capabilities also enable data collection over smaller fields of view at higher frame rates. While the possibility of acquiring time-resolved measurements has been demonstrated by Stinville et al. (38), this avenue still remains largely unexplored. The opportunities offered by these time-resolved measurements are detailed in Section 6. Implementing these techniques will certainly rely on the extensive knowledge gained from small-scale mechanical testing, as detailed in the next section.

4. ASSESSING LOCALIZED PLASTICITY AND SLIP VIA SMALL-SCALE MECHANICAL METHODS

A central question in the field of plasticity is how slip localization manifests itself in the overall deformation response. Most polycrystalline bulk crystals deform smoothly at the macroscale due to the immense, simultaneous, and spatially well-distributed dislocation activity. This in turn justifies homogenization schemes and phenomenological models that ignore any local aspects of flow, for example, as entailed in the well-known Orowan equation, $\dot{\gamma} = \rho b \bar{v}$, relating the average plastic shear strain rate to an average dislocation density ρ and velocity $\bar{v}$ and to the Burgers vector b. Single crystals instead reveal much more pronounced slip localization depending on the crystallographic loading direction, but their far-field deformation response remains smooth even in the absence of geometric constraints. In only selected cases of hcp bulk plasticity, with glide strongly confined to basal planes, can a direct signature of slip localization be resolved in a stress–strain response. This was already recognized in the early days of crystal plasticity research (160, 161). A very different picture emerges at the local scale, where the in-space heterogeneous collective dislocation activity stochastically relaxes far-field macroscopic stresses via localized shear. These local plastic processes strongly motivate small-scale deformation experiments in which slip localization becomes directly evident in force–displacement data.

Both at the bulk and small scale, the potential to assess the underlying microscopic spatiotemporal deformation physics has rarely been exploited. Instead, we have focused on the careful study of individual dislocations. At the level of temporally and spatially localized collective defect activity, we have just now started to understand how such emergent phenomena can lead to local damage signatures that exhaust the materials' loading capacity and therefore mark the initiation of macroscopic failure. This is remarkable, as many decades-old reports hint at the dominance of microplastic slip localization, which was suggested to originate from only a small part of the present dislocation population (162). To better predict and eventually mitigate localization-induced failure, it becomes imperative to be able to identify, quantify, and model the extreme events of strain and slip localization. This is a paradigm shift away from single dislocation behavior to an emergent collective behavior and has already helped in understanding grain-to-grain coupling of slip localization (163), fatigue failure initiation (164), metal shaping problems at the small scale (165), or unexpected athermal screw dislocation glide in bcc metals (166), all of which underline the important role for the non-Gaussian part of the defect activity.

In this section, we focus on two specific small-scale mechanical methods that allow probing the localization of plasticity: nanoindentation (167) and microcompression (168). We specifically address how these methods can be used to assess confined microplasticity and slip, both site-specifically and spatially across a material. Central to both methods is the benefit of statistical data sets that have the potential to uncover microstructural details, mechanisms, and mechanical properties relevant for the bulk behavior. The sketched examples are part of our vision that sufficient mechanical sampling at the small scale, and in particular sampling of localized plasticity, will allow for making well-informed predictions of both the bulk material's microstructure and its mechanical properties.

4.1. Probing Localized Plasticity with Nanoindentation

Today, automated nanoindentation is standard equipment in environments where mechanical behavior and structure–property relationships are investigated. For details on the method, the reader is referred to References 167 and 169. Instead of focusing on indentation hardness or modulus, we consider nanoindentation as a probe for localized plastic activity, which means we are paying attention to the first deviation from the elastic contact, referred to as a pop-in, which for

conospherical indentation tips is captured with a Hertzian contact model. At this point, the corresponding shear yield stress can conveniently be derived according to $\tau_y \approx A(F_p E_r^2/(\pi^3 R^2))^{1/3}$, where A is some prefactor, F_p the load at the pop-in, E_r the reduced modulus, and R the tip radius. Continued penetration of the tip into the material triggers further pop-ins, where the mechanistic origin of the local plastic instability may differ from the first pop-in. It is therefore meaningful to differentiate between the first pop-in (1, $i = 1$) and higher-order pop-ins (2, 3, 4, etc.; $i > 1$), as done in Reference 170. Below, we refer to a pop-in displacement magnitude as u_i, where i is the order.

Pop-in behavior for shallow indentation is a long-known feature that was predominantly investigated for pop-in 1, and its mechanistic origin has been ascribed to heterogeneous dislocation nucleation (171). An instructive case is Fe-3%Si, first reported by Gerberich et al. (172), who linked the abrupt strain increment to an avalanche of dislocations, the number of which depends on the yield point load F_p. Decades later, Zhang & Ohmura (173) revealed the spatial signature of the dislocation network formed at the indent site in response to the first pop-in for the same material. This extended more than a micrometer into the substrate for indents with a penetration depth of 40–50 nm. TEM evidence comparing the formed dislocation structures for only pop-in 1 and for pop-in 1 plus continued loading revealed relatively random debris for pop-in 1 alone and increasingly ordered line defects with pile-up characteristics when adding elastoplastic deformation after the pop-in. There is thus a dramatic transition in the microstructure one probes before and after the first local plastic event (174).

In addition to quantifying spatially fluctuating dislocation-nucleation or source-activation stresses from the first pop-in, appropriate thermal-activation models using statistical methods offer a way of determining the effective barrier energies of the underlying mechanisms, such as dislocation nucleation (175) or shear-band initiation in metallic glasses (176, 177). How to link the average first critical stress from a large number of indentation curves to the deforming volume and how to evaluate the underlying density of discrete plastic events from an extreme value statistics approach have also been demonstrated (178). Furthermore, recent efforts reveal that the maximum stress of the first pop-in may be linked to the material's stacking-fault energy (179). These new developments rely on quantifying spatially varying τ_y and have in common that they use statistically robust data sets from incipient and localized plasticity to determine fundamental materials properties.

Loading beyond pop-in 1, most materials admit a sequence of higher-order pop-ins, which have been neglected in the literature so far. One reason for this is the lack of an analytical expression that allows determining τ_{yi} where $i > 1$ and instead only corresponding displacements of higher-order pop-ins can be used to statistically assess how the formed dislocation network under the tip progressively evolves. In the case of the first pop-in, both τ_{y1} and u_1 are known to follow Weibull statistics (extreme value statistics) when probing a large number of point-to-point fluctuations, therefore adhering to the weakest-link picture that is compatible with heterogeneous dislocation nucleation. Interestingly, this statistical signature changes for $u_{i>1}$ to a log-normal distribution (indicative of correlated dislocation activity) in a prototypical Cu single crystal (170), demonstrating how sufficiently large data sets can discriminate between different types of localized plasticity, in this case nucleation and network evolution. How much unused potential in characterizing localized plasticity is offered by a statistical treatment of discontinuous nanoindentation data?

Figure 11*a* highlights another example of how a specific type of localized plasticity can be identified from the loading portion of a nanoindentation experiment. Instead of a first, very large pop-in followed by much smaller, higher-order pop-ins, typically seen for pure single crystalline metals, a distinct signature of continuously increasing u_i can be observed for metallic glasses (180),

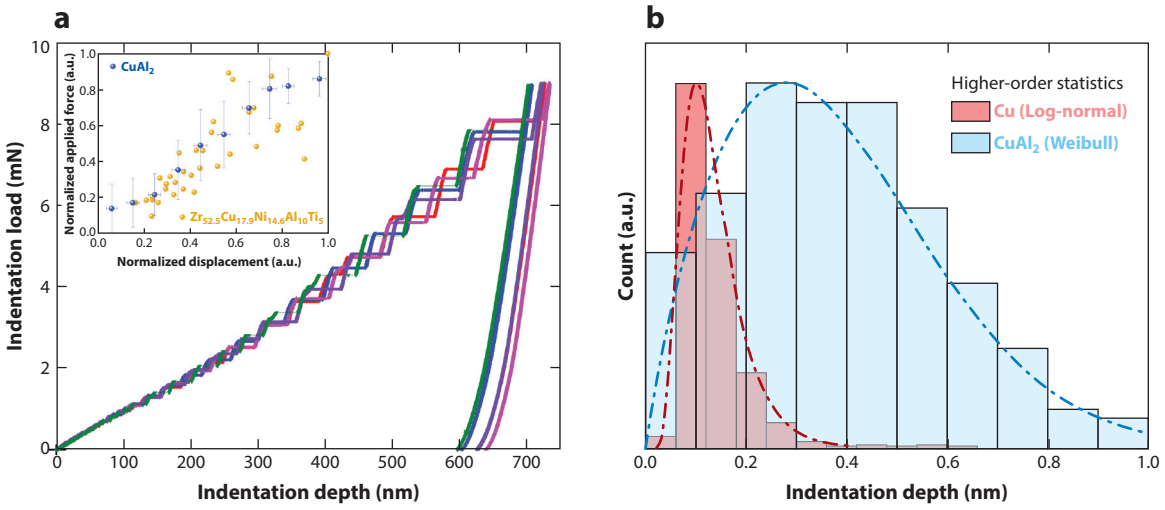

Figure 11

Slip localization probed with nanoindentation. (*a*) Four indentation curves of a $CuAl_2$ intermetallic, exhibiting an unusual continued increase of pop-in magnitude with load (182). Panel adapted from Reference 182 with permission from Elsevier. The inset displays the force–size correlation for the shown indentation curves and a Zr-based metallic glass that follows a similar trend. (*b*) A statistical analysis of the higher-order pop-in data of pure single crystalline Cu and the data shown in panel *a*, revealing fundamentally different distributions: log-normal behavior for the dislocation network evolution and Weibull statistics for shear banding.

NiPd solid solutions (181), and intermetallics (182). Specific to such data sets is that $F_i \propto u_i$ (see the inset in **Figure 11*a***), and, at least in the case of metallic glasses, it was shown that the removal of pop-in segments allows for recovering a continuation of the Hertzian elastic contact model, demonstrating essentially elastic behavior in between instabilities. This response was attributed to a geometrical scaling effect, where lines of sufficiently high shear stress around the indentation tip allow the material to deform plastically via shear localization into shear bands (183). Consequently, every newly formed shear band at a new indentation depth has a longer shear path, thereby admitting a larger pop-in size measured as an axial displacement. In fact, in the case of intermetallics, a shear-banding phenomenon could also be revealed, giving rise to the speculation that plastic localization into shear bands generally may be linked to this particular $F - u$ scaling. In direct contrast to the above-quoted, log-normally distributed higher-order pop-in displacements of pure single crystalline Cu, the continuously increasing signature of the pop-in magnitudes of the intermetallic was reported to follow Weibull statistics (**Figure 11*b***). If each instability is linked to a newly formed shear instability, this is compatible with the insight from point-to-point probed dislocation nucleation or source activation of pure metal crystals. While the available data are scarce, these results indicate the potential of revealing mechanistic information of the proceeding local plastic processes underneath the indenter from a statistical evaluation.

So far, we have considered how localization of plasticity underneath indents is giving rise to statistical data sets that are possibly unique enough for a mechanistic classification. Most of these approaches have used data sets limited to a couple of hundred indentation curves. This is expected to change, as forefront automated nanoindentation allows measurements of tens of thousands of data sets within practical time frames (184). These high-speed methods have been used mainly for hardness and indentation modulus mapping across multiphase materials, such as steel (185), concrete (186), Cu–W nanocomposites (187), and intermetallics (188). However, applying them to spatially map first- and higher-order statistics is expected to yield completely new insights into

local structure–property relationships and spatially confined plasticity, since proximities to grain and phase boundaries or dislocation cell walls are expected to affect the statistics of all signatures of localized plasticity discussed so far. Indeed, at the single-indent level, changes of the pop-in behavior near grain boundaries have already been discussed in the literature (189), where ledges in the boundaries are believed to serve as dislocation sources that can act at significantly lower stresses than within the crystal. Our expectation is that state-of-the-art high-speed nanoindentation mapping will provide deep insights into slip localization in the vicinity of grain boundaries, phase boundaries, or other microstructural features that significantly affect initiation stresses and subsequent stochastic network evolution. This thrilling avenue will provide direct insights into statistically relevant sites of early plastic activity in polycrystalline metals, constituting the next level of correlative structure–property assessment after hardness and elasticity mapping in combination with emerging machine-learning advances (190, 191).

4.2. Probing Slip Localization with Microcompression

Similar to nanoindentation, microcompression probes small volumes and therefore measures the response of single crystalline subvolumes of the polycrystalline aggregate. However, in comparison with nanoindentation, larger and finite volumes are sampled in microcompression, thereby assessing truncated bulk defect statistics that, together with exhaustion hardening and source strengthening, cause the well-known size effect in strength (192). Studying size-affected strengthening has offered mechanistic insights relevant to the micrometer and submicrometer scale, including strain-rate dependencies (193, 194) and activation volumes (194, 195), which, however, are not immediately related to strain localization. A more relevant second size effect in this context is the persistent presence of stress–strain (force–displacement) discontinuities, which are a direct signature of slip or localized plasticity. Exceeding 1% in strain for a micrometer-sized crystal, the stress–strain discontinuities may appear large, but one should not forget that the absolute magnitudes are in the nanometer range. Therefore, nanoscale intermittent slip localization due to dislocation network fluctuations cannot be resolved in bulk experimentation. Microcompression allows probing such fluctuations and, like nanoindentation, provides unique insights into specific microstructural processes.

Figure 12*a* is an exemplary depiction of a force–displacement curve obtained during microcompression of a cylindrical gold single crystal. The curve is composed of smoothly advancing segments and abrupt jumps. The smooth segments reflect, within the experimental resolution of much less than 1 nm, continuous plastic strain localization without any spatiotemporal fluctuations. A force–displacement instability, occurring at Weibull distributed stresses (196), instead signifies a collective dislocation event that mediates length changes much faster than the applied deformation rate. Much attention has been given to the non-Gaussian statistical properties of the magnitude of these abrupt slip events (197, 198), where power laws or truncated power laws describe the fluctuations we allude to in the introductory part of this section. This is remarkable, since such statistics do not have a well-defined mean, an assumption traditionally relied upon in phenomenological models. Showing various degrees of scale-free dislocation activity, the detailed functional form (power-law exponents and cut-off functions) describing the fluctuation magnitudes gives insight into the material-specific long-range correlated collective dislocation activity (199, 200) or dislocation source activity if one isolates the largest events captured by the statistics (201). Such fundamental discoveries were only possible due to small-scale deformation experiments and the ability to separately investigate intermittent slip and smooth flow, thereby demonstrating the coexistence of uncorrelated Gaussian and correlated non-Gaussian (or even scale-free) dislocation activity (166, 202).

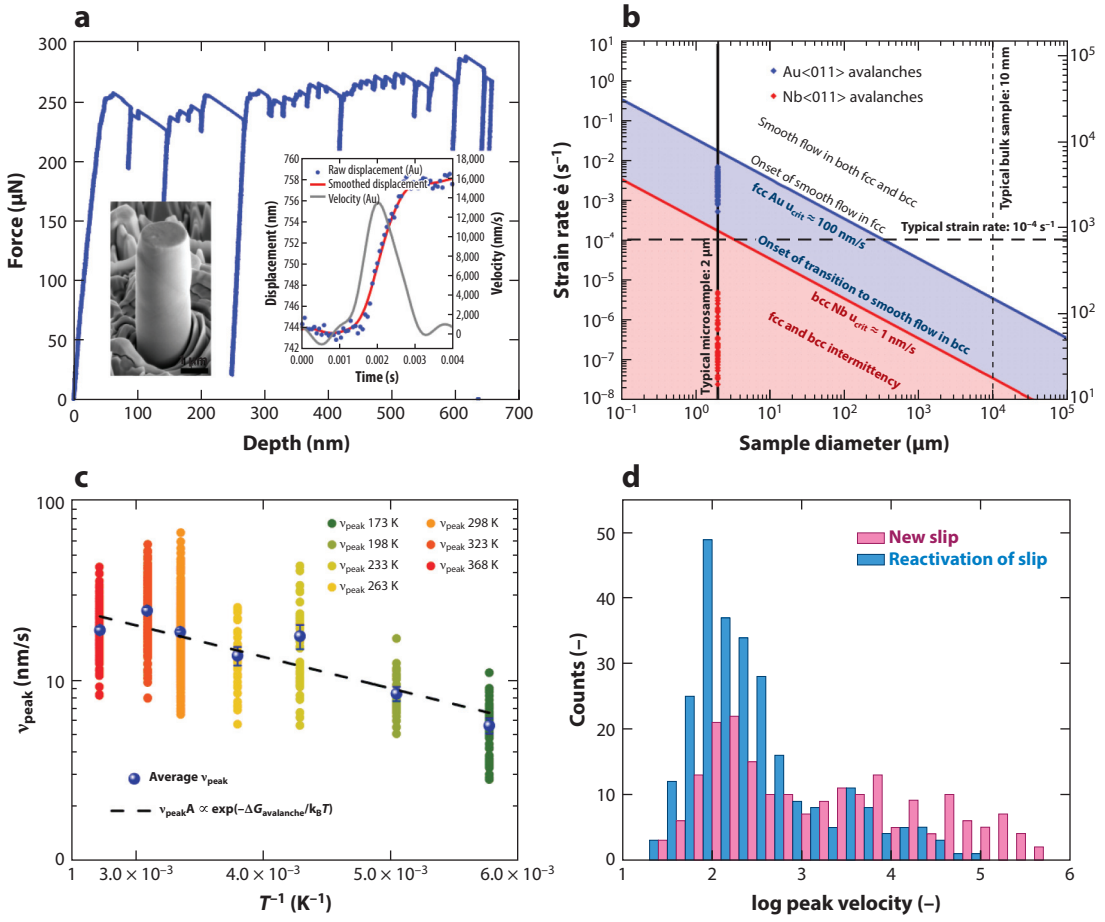

Figure 12

Insights gained from intermittent microplasticity and slip probed with microcompression. (*a*) A typical intermittent force–displacement curve for a deforming microcrystal, here being [001]-oriented Au. Panel adapted from Reference 208 with permission from Elsevier. The insets show a postdeformation scanning electron microscope image of a deformed crystal and a time-resolved profile of a displacement jump, which originates from a slip event. (*b*) A deformation map derived from both Au and Nb microcrystal deformation indicating why intermittent stress–strain behavior is not expected at the bulk scale under regular testing conditions, based on data from Reference 205. (*c*) The peak velocity of velocity profiles, as shown in the inset in panel *a*, plotted as a function of the testing temperature. An Arrhenius construction indicates essentially athermal slip. Panel adapted from Reference 166 (CC BY 4.0). (*d*) A distribution of slip peak velocities for slip on pristine slip planes and for slip for already activated slip planes. Panel adapted with permission from Reference 210; copyright 2022 American Physical Society. Abbreviations: bcc, body-centered cubic; fcc, face-centered cubic.

Going a step beyond the fluctuation magnitudes, it is possible—with experimental precautions—to derive the time-resolved signature of the collective dislocation rearrangements during slip. The inset in **Figure 12*a*** shows such a velocity profile that can be used to quantify the collective slip dynamics. The details of velocity profiles provide, if averaged sufficiently, subtle differences in how collective dislocation motion proceeds (*a*) in fcc and bcc crystals (203) or high-entropy alloys (204), (*b*) in the presence of different preexisting dislocation structures, or (*c*) due to crystal orientation (199). In fact, velocity profiles provide an answer to the question of why the spatiotemporal slip fluctuations of **Figure 12*a*** are not seen in a general bulk experiment: Despite large scatter, peak velocities of the collective dynamics are finite, meaning they can couple

to the externally applied rate. **Figure 12*b*** summarizes this based on the data for Au and Nb microcrystals (205), outlining sample-size dependent transition regimes in strain rate. Since a given strain rate becomes an increasingly large absolute deformation rate, a situation will arise with increasing sample size in which the underlying collective dynamics enters driven slip deformation. This time scale and rate competition offer a rationale for the absence of similar plastic stress–strain fluctuations in typical bulk experiments. Even though the deformation map in **Figure 12*b*** ignores the effect of the surface-to-volume ratio or the presence of internal truncation length scales, this interpretation aligns well with the transition from serrated to nonserrated flow of bulk metallic glasses (206) or dynamic strain aging (207).

Another way of exploiting the independent accessibility of smooth, presumably Gaussian, dislocation activity and the correlated non-Gaussian component is to track the spatiotemporal slip dynamics across temperature. This has recently revealed the coexistence of athermal and thermally activated screw-dislocation plasticity in a bcc lattice (166). With decreasing deformation temperature, Nb evidences an almost unaltered slip velocity of the collective events, which is demonstrated in **Figure 12*c*** in the form of an Arrhenius construct that returns an effective barrier energy of approximately 0.04 eV. This is an order of magnitude lower than what is derived from the smooth deformation component of the same experiments (209) and raises the question of whether there is a fundamental bimodality in the dislocation network evolution during slip. Relying on DDD simulations, compelling evidence for athermal screw-dominated slip avalanches in highly stressed regions was found. In these local environments of high stress, the Peierls potential is no longer the rate-limiting factor during collective dislocation rearrangement.

These briefly sketched examples demonstrate how a micromechanical experiment and the tracking of localized slip can provide novel insights into deformation mechanisms that are relevant for bulk plasticity. A question that has been ignored so far is how slip localization extends spatially in the probed volume. Any stress–strain instability reveals only the net displacement magnitude, and gleaned from postmortem slip line analysis, an implicit assumption of single slip plane activation has prevailed. As recently shown via in situ experimentation (210), a single stress–strain instability can originate from a multitude of complex slip processes involving one to many different slip planes, even though the net magnitude is the same. This clearly demonstrates how a population of dislocation sources with sufficiently close strengths is present such that not only the weakest source becomes active, which would result in highly localized slip on one given slip plane. Furthermore, it was found that large fast slip events are linked to the activation of previously inactive slip planes, whereas reactivation mediates smaller slip magnitudes at a slower rate. **Figure 12*d*** demonstrates this for slip localization in an fcc solid-solution high-entropy alloy (210), implying that any dislocation debris left behind after slip suppresses subsequent slip dynamics. While at first glance, this might seem to be a finding of purely fundamental value, the immediate relevance to structural stability and failure becomes clear when considering that the suppression of fast collective dynamics directly translates to a suppression of the extreme events that give rise to the non-Gaussian power-law statistics. Being nothing more than a hypothesis at this point, it is very likely that collective-correlated dislocation dynamics (i.e., avalanches) with a high net Burgers vector content give rise to slip localization that leads to strong internal stress fluctuations and concentrations. This has, in fact, been suggested on the basis of cyclic loading, where strongly non-Gaussian components of the strain localization could be linked to microcrack initiation (211). If correct, extreme events of strain localization should come into focus when designing damage tolerant alloys. What kind of obstacles, and therefore structure–property relationships, are the most efficient to suppress these rare but extreme strain localization events remains unclear, as complex microstructures including grain boundaries, solid solutions, precipitates, and irradiation structures continue to bear their signatures (202, 212–214). Being a powerful method to directly

track strain localization due to (weakly) correlated dislocation activity, microcompression will continue to play a central role in unraveling the details of spatially confined plasticity and slip, as well as their relationship to local failure initiation.

5. MODELING SLIP LOCALIZATION

5.1. Modeling Techniques for Slip Localization

Modeling subgranular slip localizations with most conventional deformation models, even the most mechanically sophisticated, is challenging. First, the discrete nature of slip localization is inherently inhomogeneous, rendering most classical micromechanical formulations inapplicable. Second, intensification of slip is naturally a multiscale process, initiating at some fine nanoscale region and extending across the grain before intensifying to detectable levels at the micrometer scale and larger. Application of standard coarse-graining modeling techniques for slip localization can, therefore, be problematic. Finally, slip localization events do not occur in isolation. Mutual interactions with other slip localization processes at variable distances within the same grain or in the neighboring grains can affect their development.

CP theory has served as a basis for modeling slip localization. Of the many polycrystalline deformation modeling tools, the ones that best meet the challenges above combine CP and a full-field mechanical approach, such as the finite element method (CP-FE) or an FFT scheme (CP-FFT) (215, 216). These models require as input an explicit, spatially resolved description of the material microstructure (e.g., grain connectivity, shape, relative size, orientation) and return the spatially resolved mechanical response and strain evolution of the grain structure. As another asset for modeling slip localization formation, for every compute point, inside every grain, these models determine crystallographic slip activity while under the constraint of deforming neighboring grains.

In all such models, a nonnegative, nonzero stress, denoted by τ, for activating slip in the grains must be prescribed. Traditionally, it is presumed that τ does not change or increase with the rate of slip. To model the formation of slip localization, however, most models adopt a softening law for τ. Softening means that τ decays with increasing amounts of slip and, when applied to slip localization, is intended to represent the consequence of heat generation due to dissipation of the plastic work that is performed by the several fast-moving, like-signed dislocations in the slip localization. Some models predefine a planar region inside the model grain(s) wherein τ decreases with the slip rate (217, 218) (**Figure 13*a*,*c***). Other models allow the degree of softening to depend on the amount of accumulated slip with no assumptions on localization paths (13) (**Figure 13*b***). Alternatively, the model by Ahmadikia et al. (218) introduced a crystallographic planar region in which slip was permitted to localize, and whether localization occurred depended on the material, microstructure, and loading intensity and direction (**Figure 13*c***).

5.2. Correlation with Experimental Measurements and Observations

Slip localizations are modeled at the subgranular scale, enabling direct comparison with surface measurements of slip localizations in deformed materials. Because microstructural information below the surface is commonly lacking, 3D modeled microstructures often choose to extend the surface structure in the out-of-plane direction, creating a columnar structure. **Figure 14*a*** shows the measured strain accumulated across a slip localization obtained from HR-DIC. The amount of accumulated peaks in the center of the grain is lowest where the slip localization meets the grain boundaries. For the same microstructure, the model applies the same strain-state far field by starting from zero and building it up at the same rate as in the experiment. The grains initially deform homogeneously but eventually slip localize. At the same level (0.61% strain), the accumulated slip profile across the slip localization calculated by the model agrees with the measured

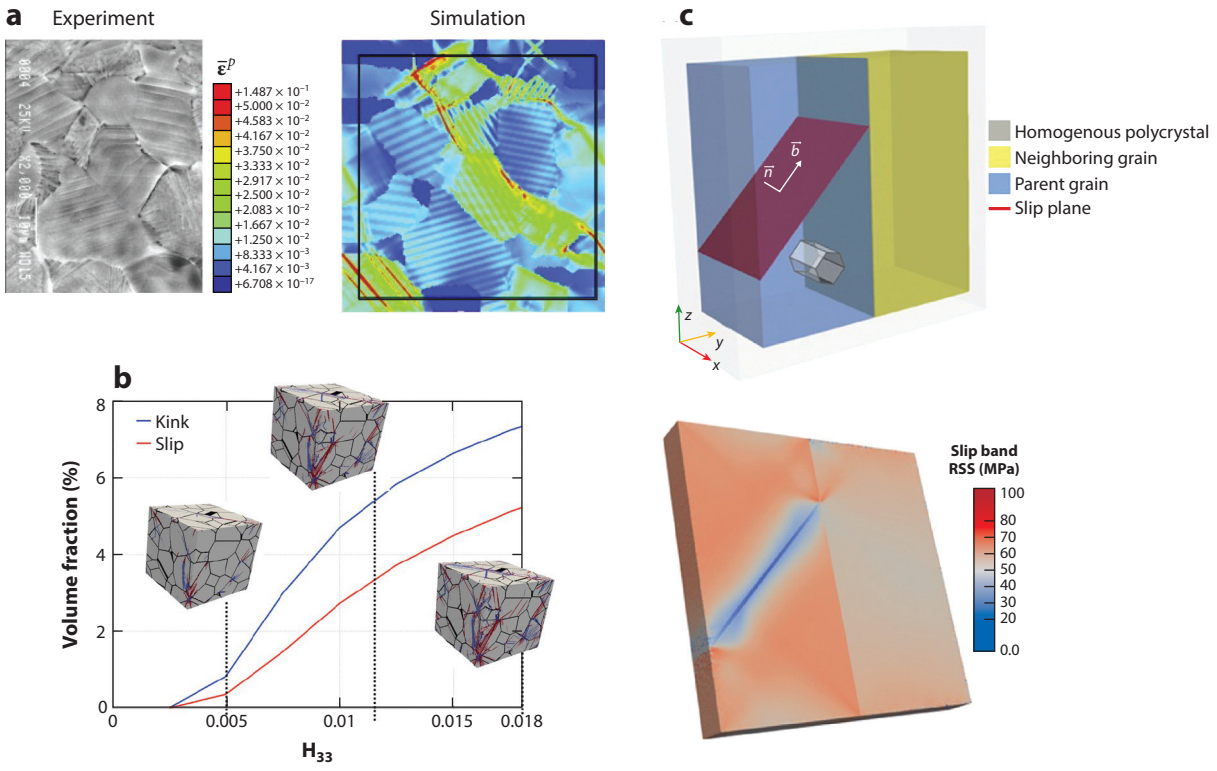

Figure 13

(*a*) Modeling of slip localization using crystal plasticity simulations shows regions of planar slip within grains, also observed in the experiment. Panel adapted from Reference 217 with permission from Elsevier. (*b*) Pathways for localization during deformation (slip and kinking) are mapped by massively parallel fast Fourier transform simulations. Panel adapted from Reference 13 with permission from Elsevier. (*c*) A region of finite thickness is introduced in which a slip band is eligible to form. If the material and external conditions are suitable, for instance, the resolved shear stress (RSS) on a slip band, a slip could localize in this region. Panel adapted from Reference 218 with permission from Elsevier.

one. The predicted local stress fields indicate that the neighboring grains resist the shear imposed by slip localization and react by generating a back stress in the grain with the slip localization. The back stress is strongest at the slip localization–grain boundary junction. This back stress can prevent neighboring slip localizations from developing within the same grain.

The stress concentrations that develop ahead of a slip localization in the neighboring grain can cause slip systems and other deformation mechanisms that would not otherwise occur or are unexpected. One example that has been studied is deformation twinning (216, 219). The character of the localized stress from the localization can trigger twins of variants that would not be preferred by average stress in the grain. In some rare instances, a 3D feature called a microvolume (105, 106) forms in a grain neighboring another grain containing a slip localization (**Figure 6*b*,*c***). It is characterized as a local plume-shaped zone encompassing large stresses and lattice rotations and is associated with slip localizations that tend to nucleate cracks in cyclic loading (33, 220). With the experimental microstructure, the CP-FE slip localization model by Latypov et al. (221) predicted the formation of microvolumes of similar extent and amount of reorientation in the neighboring grain as seen experimentally (**Figure 14*b***). By combining these calculations with other simulations for alternative, hypothetical neighboring grain orientations, the analysis showed

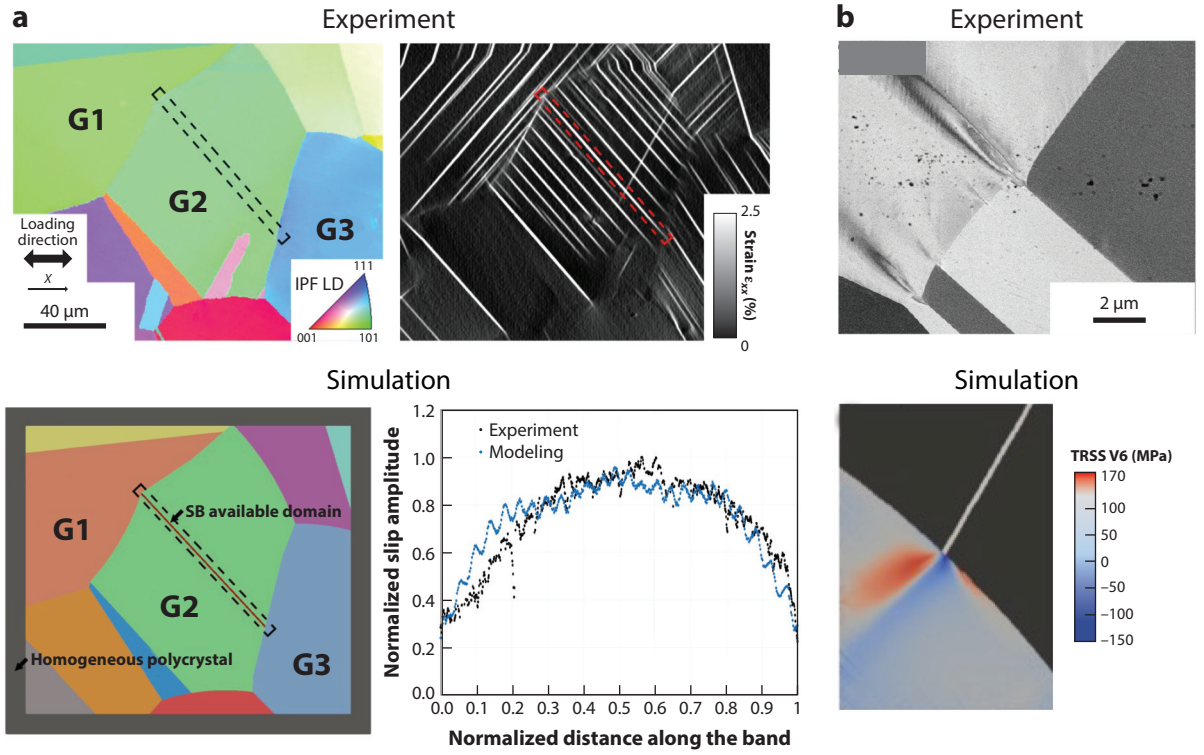

Figure 14

Correlation between experimental and numerical measurements. (*a*) Experimentally captured microstructure is used as input. The slip localization event is explicitly described in a crystal plasticity simulation. The slip intensity along the profile of the slip event is accurately captured by the model. Panel adapted from Reference 218 with permission from Elsevier. (*b*) Crystal plasticity model permitting the development of an explicit slip event predicted the onset of SB formation and its development in intensity as a result of the parent orientation and surrounding neighboring grains. This blocked SB induces significant stress and lattice rotation in the neighboring grain. Panel adapted from Reference 218 with permission from Elsevier. Abbreviations: IPF, inverse pole figure; LD, loading direction; SB, slip band; TRSS, twin-plane resolved shear stress.

that microvolumes form when the slip localization is exceptionally intense and the neighboring grain orientation responds by activating multiple slip systems within the microvolume.

Although slip localization is confined to form within a crystallographic slip plane of a grain, the slip localization in different grains can appear to link up across grain boundaries, forming a piecewise chain that can span from 2 to 20 grains (59). CP simulations allowing for slip localization to possibly form in one grain while being bounded to other grains have been conducted (218). The comparison with observation revealed that the propensity for slip localization in one grain strongly depends on the orientation of its neighboring grains. For high-angle grain boundaries, the slip localization is weak, signifying that grain deformation occurs homogeneously throughout the grain. For low-angle grain boundaries, intense slip localization is promoted, achieving strain levels like those seen experimentally.

5.3. Theoretical Understanding of Slip Localization

The latest advances in slip localization modeling have revealed the important influence of material and microstructural properties. The models have proven helpful in isolating the roles of one

property among the many degrees of freedom that are associated with material and microstructure. Two examples are discussed below.

The plastic deformation of grains in hcp materials is anisotropic, sensitive to the lattice orientation of the grain. If a grain is oriented such that the stress must drive a hard mode of slip and thus is hard to plastically deform, then its orientation is a so-called hard orientation. A soft orientation is the opposite, wherein the stress activates the easier slip modes, which are usually basal or prismatic modes. In high-performance hcp alloys, such as those based on Ti or Mg, slip localizations are most often aligned with the basal or prismatic modes (59, 222). A simple bicrystal model was set up with the parent grain allowing either a basal or prismatic slip localization to form when stressed and a neighboring grain of arbitrary orientation (218). The calculation of the critical strain to localization ϵ_{loc}, in which the slip localization sustains twice the strain as the rest of the grain, was repeated for the full space of orientations for the neighboring grains. The relatively harder neighbors resisted the slip localization, causing a larger back stress in the parent grain in the vicinity of but outside the slip localization. The back stress lowers the driving force for new slip localizations in the parent grain, encouraging the slip localization to accommodate even further increases in applied deformation.

Shortly after yielding, strong polycrystalline materials usually exhibit some amount of strain hardening, defined as an increase in flow stress with deformation. Concomitantly, the local slip strength τ to activate slip in the grains increases with strain as well. Higher values of τ are usually associated with stronger materials. With a simple bicrystal model for slip localization, the competition between hardening in the parent grain volume and local softening in its slip localization and the role of τ were investigated.

Compared with commercially pure Ti (CP-Ti), Mg is the weaker material, wherein the local τ to activate slip in any of the slip modes in Mg is lower than that in CP-Ti (216, 223). Slip localization calculations found that Mg requires substantially higher ϵ_{loc} for the onset of localization and accumulates less strain within the slip localization than the stronger material, CP-Ti. For some grain neighbor orientations in Mg, slip localization did not even form within the 1% applied strain, indicating that conditions do exist where slip localization is not preferred over homogeneous slip in the grain. Further, with the model, the role of elastic anisotropy can be isolated. It was shown that the stronger elastic anisotropy in CP-Ti, compared with that in Mg, contributes to the accumulation of more strain in the slip localization in CP-Ti.

6. FUTURE CHALLENGES

In this article we highlight two broad experimental approaches to elucidate the effect of microstructure on slip localization to improve our understanding of the mechanical properties of metallic materials. The first set of approaches (Section 2) quantifies individual slip event characteristics across a range of length scales for fixed deformation states. The second approach (Section 4) consists of dynamically probing the overall evolution of plasticity during deformation of small-scale specimens, targeting unique microstructure features.

A direction of interest lies in evolving these approaches to capture the dynamics of single slip events over large representative areas or volumes of the microstructure. To accomplish this, expanding the described advanced experimental tools using autonomous, integrated, and high-throughput techniques is necessary. High-throughput measurements of deformation processes at the nanometer scale are critical for providing statistical measurements that are representative of multiscale hierarchical microstructures while describing the active deformation mechanisms. With the emergence of techniques such HR-DIC measurements or ECCI imaging, statistical measurement of individual deformation events can be performed on a large sampling area or

volume. The development of HR-DIC measurements inside the SEM is an excellent example of the statistical analysis of physical deformation mechanisms.

However, the measurement acquisition times of these techniques are on the order of a few days for fields of view larger than a square millimeter that capture the microstructure heterogeneity. The need for high-throughput, multimodal (chemical, crystallographic, phase morphology) characterization will continue to motivate the development of new characterization platforms. A recent example is evident in 3D microstructure characterization, where novel technological developments for in situ material removal such as femtosecond laser ablation and plasma focused ion beam milling (86) have been motivated by the need for high-resolution, multimodal data. EBSD data collection needs to be accelerated to allow acquisition of cubic millimeter data sets with submicrometer resolution in a matter of hours. In this context, emerging fast direct electron detecting EBSD technologies are an appealing option (80). Another way to decrease measurement time for statistical analysis is using automation tools. An example can be found in 3D microstructure measurements using the Robo-Met 3D (85) where robotic platforms are used to automate measurements. Moreover, the recent developments of scripting procedures that allow automation of SEMs and in situ mechanical loading stages and new SEM imaging technologies, such as the multibeam technology, are other examples of the acceleration of material characterization (223a). Using microscope scripting procedures during HR-DIC measurements, the evolution of slip localization during dwell hold of a titanium alloy was captured dynamically at the scale of the second (38) (**Figure 15**). Increases in temporal resolution to capture the evolution of discrete deformation events over large fields in polycrystalline materials may provide a better understanding of these deformation events and the role of the microstructure.

High-performance materials for use in extreme environments will likely deform via other deformation modes, such as deformation twinning or grain boundary sliding. Stress concentrations arising from slip localization result in a complex interplay between deformation mechanisms; these interplays are challenging to capture with existing experimental or numerical tools.

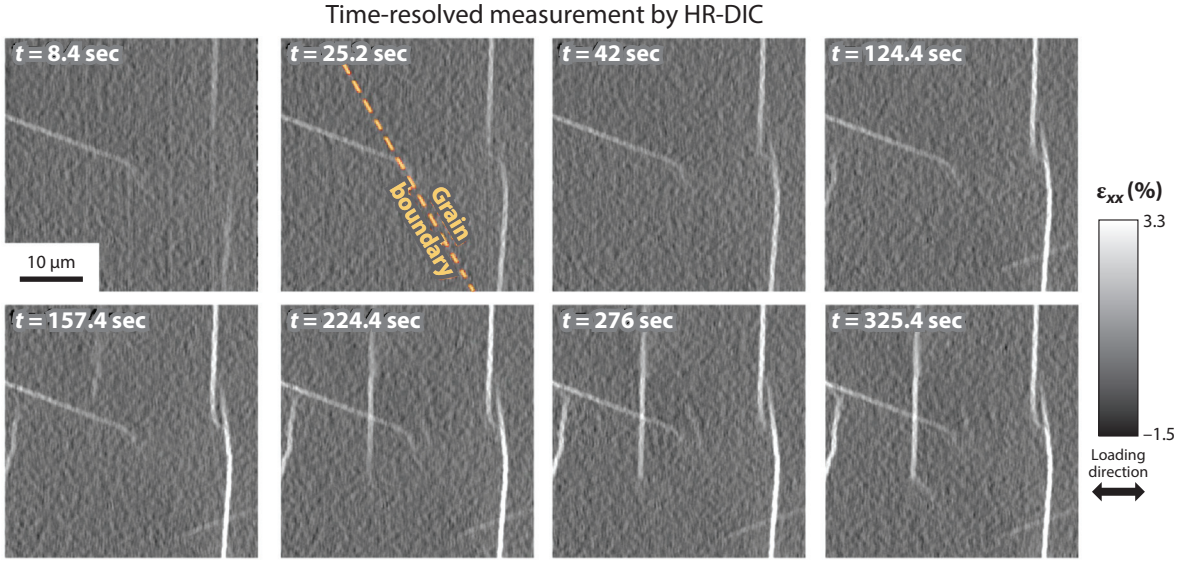

Figure 15

Time-resolved high-resolution digital image correlation (HR-DIC) during a dwell time interval in a titanium alloy. Figure adapted from Reference 38 with permission of Springer Nature.

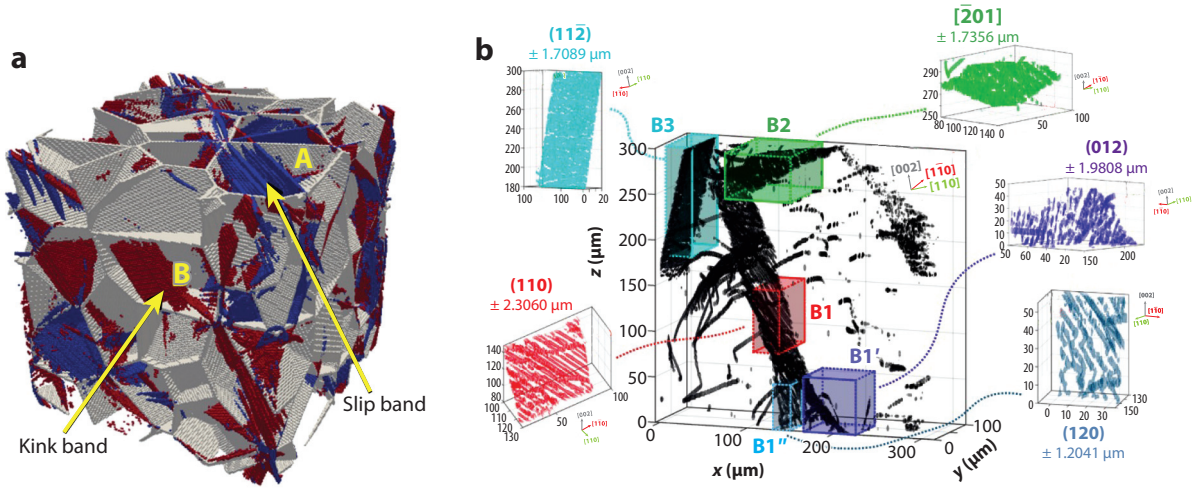

Figure 16

(*a*) Numerical prediction of kink and slip band by softening crystal plasticity fast Fourier transformation simulations. Panel adapted from Reference 13 with permission from Elsevier. (*b*) Large bulk 3D volume of dislocation structures using dark-field X-ray microscopy. Subgrains separated by dislocation boundaries are identified down to the single-dislocation level using computer vision methods. Panel *b* adapted from Reference 224 (CC BY 4.0).

However, significant efforts are being made to adapt these tools. For instance, discontinuity-tolerant HR-DIC codes have been adapted to quantify deformation slip and can be implemented to identify deformation twinning. In this example, the Heaviside-DIC code provides automatic identification and quantification from deformation and strain fields of slip and twin deformation events. Such approaches are also being developed on the numerical side to capture the activation of different deformation mechanisms such as kink band or deformation slip (**Figure 16*a***).

Slip localization events are usually investigated at the surface of the specimen. With the use of new experimental measurements, such as X-ray bulk measurement (9), 3D correlative measurements and numerical analysis (46), or high-resolution measurements (107), information on slip localization can be obtained from the subsurface or within the bulk of the material. For instance, different slip localization behaviors have been observed at the surface compared with in the bulk (9); elucidating these differences will be critical to our understanding of mechanical properties in engineered components. In parallel, increases in spatial resolution in synchrotron-based measurements now allow the capturing of individual plastic events in the bulk (**Figure 16*b***). These capabilities will further explain the differences in deformation mechanisms between the surface and bulk.

The one-to-one comparison of 3D experimental and numerical predictions, as shown in **Figures 14** and **16**, will significantly accelerate our understanding of the effect of highly heterogeneous plastic flow and the resultant chains of events that affect bulk mechanical properties. This understanding will further inform the infrastructure for digital twins (225). In addition, with the experimental capture of the physical characteristics of the slip localization events over representative regions, identification of critical microstructural configurations is possible, and small-scale or/and multiscale modeling can be achieved on these configurations to highlight deformation mechanisms at the small scale. For instance, a one-to-one comparison of surface displacement fields between DDD simulations (226) and HR-DIC measurements may provide a better understanding of dislocation mechanisms that lead to slip localization.

Overall, the innovative experimental and numerical approaches being developed are incorporating more physical considerations of slip localization, such as the explicit description of slip localization in CP simulation (**Figures 13** and **14**) or discontinuities analysis in HR-DIC (**Figure 1**). The use of forward models is therefore of relevance and can better explain the signatures of slip localization. An example is the development of EBSD forward models for the identification of defect (87). With high-speed and high-resolution direct electron detectors and coupled forward modeling, there are opportunities to explore dislocation content and other features (beyond just crystal orientation) that are embedded within an EBSD Kikuchi pattern (88). For X-ray measurements of slip localization, the development of forward models is in progress. These models are especially important since bulk measurements are more convoluted than surface ones, and the use of forward models to retrieve additional quantities (local lattice rotation and strains, for instance) and increase spatial resolution is a very promising route.

Each measurement technique has its own unique advantages and enabling correlative multimodal acquisition schemes is key for gathering the right amount of information at the right scale. Over time, we can anticipate that a more physically based mechanical description of these phenomena can be reached and deployed in a multi-scale framework for use in optimizing material properties. With the rise of multimodal, correlative, and statistical measurements of large surfaces or volumes with nanometer resolution comes data management and analysis issues. Significant effort remains to develop and adapt tools for big data management and analysis.

The continued development of experimental, numerical, and data analysis tools to capture slip localization as a function of the multiscale microstructure or chemical composition in metallic materials promises significant strides in our predictive capabilities of mechanical properties that will accelerate the design of new alloys.

SUMMARY POINTS

1. Emerging experimental and computational techniques are expanding our understanding of slip localization.
2. Strain measurements by high-resolution digital image correlation show an intrinsic link between plastic localization in metallic materials at the nanometer scale and macroscopic mechanical properties.
3. Quantitative multimodal data fusion has been demonstrated to link plastic localization measurements at the surface to subsurface microstructural features.
4. All electron backscatter diffraction (EBSD) techniques (e.g., high-resolution EBSD, 3D EBSD) are poised for substantial improvements in speed, orientation resolution, and detector efficiency due to nonphosphor coupled direct electron detectors.
5. X-ray imaging techniques (topotomography, dark-field X-ray microscopy) are scaling to volumes that can probe deformation and localization in the bulk, providing crucial comparisons to the more ubiquitous surface strain measurements.
6. Small-scale plasticity in combination with statistical data assessment reveals novel mechanistic insights into localized plasticity and slip activity that bulk experimentation cannot provide.
7. New in situ imaging modality by a transmission scanning electron microscope allows the determination of the dynamics of dislocations that lead to plastic localization.

8. Recent advancements in crystal plasticity modeling demonstrate the ability to model the development of intragranular slip localizations with strain. They reveal the propensity for slip localization as a function of material strength and immediate grain neighborhood.

FUTURE ISSUES

1. Automation of data fusion would enable multimodal and temporal measurements over larger volumes, providing statistically relevant data sets for mining microstructure–property linkages.
2. Materials with more diffuse and nonlocalizing deformation modes, or with a multitude of these modes, present new challenges for understanding plastic deformation behavior.
3. How microstructural variations statistically affect incipient plasticity and dislocation avalanche properties, and how these can be used to quantify dislocation mechanisms, remains largely unexplored.
4. The link between large spatially resolved plasticity data sets from automated nanoindentation and representative bulk properties is yet to be established.
5. Explicit modeling of slip localizations in large-scale polycrystal simulations can help accelerate microstructural design for improved strength and lifetime.

DISCLOSURE STATEMENT

The authors are not aware of any affiliations, memberships, funding, or financial holdings that might be perceived as affecting the objectivity of this review.

ACKNOWLEDGMENTS

J.C.S. and M.A.C. are grateful for financial support from the start-up fund from the Department of Materials Science and Engineering at the University of Illinois, Urbana-Champaign (UIUC). I.J.B., T.M.P., J.C.S., and M.A.C. are grateful for the support of the US Department of Energy, Office of Basic Energy Sciences Program (DE-SC0018901). R.M. is grateful for financial support from the National Science Foundation's CAREER program (grant NSF DMR 1654065) and for funds provided by the Department of Materials Science and Engineering at UIUC and the Federal Institute of Materials Research and Testing (BAM). P.G.C. would like to acknowledge support provided by the Naval Research Laboratory under the auspices of the Office of Naval Research.

LITERATURE CITED

1. Tatschl A, Kolednik O. 2003. A new tool for the experimental characterization of micro-plasticity. *Mater. Sci. Eng. A* 339:265–80
2. Stinville JC, Echlin MP, Texier D, Bridier F, Bocher P, Pollock TM. 2016. Sub-grain scale digital image correlation by electron microscopy for polycrystalline materials during elastic and plastic deformation. *Exp. Mech.* 56:197–216
3. Magazzeni CM, Gardner HM, Howe I, Gopon P, Waite JC, et al. 2021. Nanoindentation in multimodal map combinations: a correlative approach to local mechanical property assessment. *J. Mater. Res.* 36:2235–50

4. Jelinek A, Zak S, Alfreider M, Kiener D. 2022. High-throughput micromechanical testing enabled by optimized direct laser writing. *Adv. Eng. Mater.* 25:2200288
5. Zhang X, Xiang Y. 2017. Combinatorial approaches for high-throughput characterization of mechanical properties. *J. Materiomics* 3:209–20
6. Eastman DW, Shade PA, Uchic MD, Hemker KJ. 2020. Microscale testing and characterization techniques for benchmarking crystal plasticity models at microstructural length scales. In *Integrated Computational Materials Engineering (ICME)*, ed. S Ghosh, C Woodward, C Przybyla, pp. 91–125. Cham, Switz.: Springer Int.
7. Moore S, Burrows R, Kumar D, Kloucek MB, Warren AD, et al. 2021. Observation of stress corrosion cracking using real-time in situ high-speed atomic force microscopy and correlative techniques. *NPJ Mater. Degrad.* 5:3
8. Proudhon H, Guéninchault N, Forest S, Ludwig W. 2018. Incipient bulk polycrystal plasticity observed by synchrotron in-situ topotomography. *Materials* 11. **https://doi.org/10.3390/ma11102018**
9. Stinville J, Ludwig W, Callahan P, Echlin M, Valle V, et al. 2022. Observation of bulk plasticity in a polycrystalline titanium alloy by diffraction contrast tomography and topotomography. *Mater. Charact.* 188:111891
10. Jakobsen A, Simons H, Ludwig W, Yildirim C, Leemreize H, et al. 2019. Mapping of individual dislocations with dark-field X-ray microscopy. *J. Appl. Crystallogr.* 52:122–32
11. Stinville J, Vanderesse N, Bridier F, Bocher P, Pollock T. 2015. High resolution mapping of strain localization near twin boundaries in a nickel-based superalloy. *Acta Mater.* 98:29–42
12. Boyce BL, Uchic MD. 2019. Progress toward autonomous experimental systems for alloy development. *MRS Bull.* 44:273–80
13. Marano A, Gélébart L, Forest S. 2019. Intragranular localization induced by softening crystal plasticity: analysis of slip and kink bands localization modes from high resolution FFT-simulations results. *Acta Mater.* 175:262–75
14. Burnett TL, Withers PJ. 2019. Completing the picture through correlative characterization. *Nat. Mater.* 18:1041–49
15. Lenthe WC, Echlin MP, Trenkle A, Syha M, Gumbsch P, Pollock TM. 2015. Quantitative voxel-to-voxel comparison of TriBeam and DCT strontium titanate three-dimensional data sets. *J. Appl. Crystallogr.* 48:1034–46
16. Polonsky AT, Pandey A. 2021. Advances in multimodal characterization of structural materials. *JOM* 73:3228–29
17. Kalidindi SR, Buzzy M, Boyce BL, Dingreville R. 2022. Digital twins for materials. *Front. Mater.* 9:818535
18. Allison J, Backman D, Christodoulou L. 2006. Integrated computational materials engineering: a new paradigm for the global materials profession. *JOM* 58:25–27
19. Stinville JC, Charpagne MA, Cervellon A, Hemery S, Wang F, et al. 2022. On the origins of fatigue strength in crystalline metallic materials. *Science* 377:1065–71
20. Dawson PR, Miller MP, Pollock TM, Wendorf J, Mills LH, et al. 2021. Mechanical metrics of virtual polycrystals (MechMet). *Integrat. Mater. Manuf. Innov.* 10:265–85
21. Harte A, Atkinson M, Smith A, Drouven C, Zaefferer S, et al. 2020. The effect of solid solution and gamma prime on the deformation modes in Ni-based superalloys. *Acta Mater.* 194:257–75
22. Weidner A, Biermann H. 2021. Review on strain localization phenomena studied by high-resolution digital image correlation. *Adv. Eng. Mater.* 23:2001409
23. Montgomery C, Koohbor B, Sottos N. 2019. A robust patterning technique for electron microscopy-based digital image correlation at sub-micron resolutions. *Exp. Mech.* 59:1063–73
24. Hoefnagels J, van Maris M, Vermeij T. 2019. One-step deposition of nano-to-micron-scalable, high-quality digital image correlation patterns for high-strain in-situ multi-microscopy testing. *Strain* 55:e12330
25. Kammers A, Daly S. 2013. Self-assembled nanoparticle surface patterning for improved digital image correlation in a scanning electron microscope. *Exp. Mech.* 53:1333–41
26. Sutton MA, Li N, Garcia D, Cornille N, Orteu JJ, et al. 2006. Metrology in a scanning electron microscope: theoretical developments and experimental validation. *Meas. Sci. Technol.* 17:2613–22

27. Lenthe WC, Stinville JC, Echlin MP, Chen Z, Daly S, Pollock TM. 2018. Advanced detector signal acquisition and electron beam scanning for high resolution SEM imaging. *Ultramicroscopy* 195:93–100
28. Hémery S, Stinville J, Wang F, Charpagne M, Emigh M, et al. 2021. Strain localization and fatigue crack formation at (0001) twist boundaries in titanium alloys. *Acta Mater*. 219:117227
29. Arani MM, Ramesh N, Wang X, Parson N, Li M, Poole W. 2022. The localization of plastic deformation in the precipitate free zone of an Al-Mg-Si-Mn alloy. *Acta Mater*. 231:117872
30. Atkinson MD, Donoghue JM, da Fonseca JQ. 2020. Measurement of local plastic strain during uniaxial reversed loading of nickel alloy 625. *Mater. Charact.* 168:110561
31. Xu X, Lunt D, Thomas R, Babu RP, Harte A, et al. 2019. Identification of active slip mode in a hexagonal material by correlative scanning electron microscopy. *Acta Mater*. 175:376–93
32. Harr M, Daly S, Pilchak A. 2021. The effect of temperature on slip in microtextured Ti-6Al-2Sn-4Zr-2Mo under dwell fatigue. *Int. J. Fatigue* 147:106173
33. Stinville J, Callahan P, Charpagne M, Echlin M, Valle V, Pollock T. 2020. Direct measurements of slip irreversibility in a nickel-based superalloy using high resolution digital image correlation. *Acta Mater*. 186:172–89
34. Vermeij T, Hoefnagels J. 2022. Plasticity, localization, and damage in ferritic-pearlitic steel studied by nanoscale digital image correlation. *Scr. Mater.* 208:114327
35. Vermeij T, Verstijnen JAC, Ramirez y Cantador TJJ, Blaysat B, Neggers J, Hoefnagels JPM. 2022. A nanomechanical testing framework yielding front&rear-sided, high-resolution, microstructure-correlated SEM-DIC strain fields. *Exp. Mech.* 62:1625–46
36. Jiang R, Pierron F, Octaviani S, Reed P. 2017. Characterisation of strain localisation processes during fatigue crack initiation and early crack propagation by SEM-DIC in an advanced disc alloy. *Mater. Sci. Eng. A* 699:128–44
37. Guery A, Hild F, Latourte F, Roux S. 2016. Slip activities in polycrystals determined by coupling DIC measurements with crystal plasticity calculations. *Int. J. Plast.* 81:249–66
38. Stinville JC, Francis T, Polonsky AT, Torbet CJ, Charpagne MA, et al. 2021. Time-resolved digital image correlation in the scanning electron microscope for analysis of time-dependent mechanisms. *Exp. Mech.* 61:331–48
39. Di Gioacchino F, Quinta da Fonseca J. 2013. Plastic strain mapping with sub-micron resolution using digital image correlation. *Exp. Mech.* 53:743–54
40. Chen Z, Daly S. 2018. Deformation twin identification in magnesium through clustering and computer vision. *Mater. Sci. Eng. A* 736:61–75
41. Chen Z, Lenthe W, Stinville JC, Echlin M, Pollock TM, Daly S. 2018. High-resolution deformation mapping across large fields of view using scanning electron microscopy and digital image correlation. *Exp. Mech.* 58:1407–21
42. Linne MA, Bieler TR, Daly S. 2020. The effect of microstructure on the relationship between grain boundary sliding and slip transmission in high purity aluminum. *Int. J. Plast.* 135:102818
43. Linne MA, Daly S. 2019. Data clustering for the high-resolution alignment of microstructure and strain fields. *Mater. Charact.* 158:109984
44. Edwards TEJ, Di Gioacchino F, Clegg WJ. 2021. High resolution digital image correlation mapping of strain localization upon room and high temperature, high cycle fatigue of a TiAl intermetallic alloy. *Int. J. Fatigue* 142:105905
45. Charpagne MA, Stinville JC, Polonsky AT, Echlin MP, Pollock TM. 2021. A multi-modal data merging framework for correlative investigation of strain localization in three dimensions. *JOM* 73:3263–71
46. Charpagne M, Hestroffer J, Polonsky A, Echlin M, Texier D, et al. 2021. Slip localization in Inconel 718: a three-dimensional and statistical perspective. *Acta Mater*. 215:117037
47. Sperry R, Han S, Chen Z, Daly SH, Crimp MA, Fullwood DT. 2021. Comparison of EBSD, DIC, AFM, and ECCI for active slip system identification in deformed Ti-7Al. *Mater. Charact.* 173:110941
48. Edwards TEJ, Maeder X, Ast J, Berger L, Michler J. 2022. Mapping pure plastic strains against locally applied stress: revealing toughening plasticity. *Sci. Adv.* 8:eabo5735
49. Bourdin F, Stinville J, Echlin M, Callahan P, Lenthe W, et al. 2018. Measurements of plastic localization by heaviside-digital image correlation. *Acta Mater*. 157:307–25

50. Chen Z, Daly S. 2017. Active slip system identification in polycrystalline metals by digital image correlation (DIC). *Exp. Mech.* 57:115–27
51. Bergsmo A, Xu Y, Poole B, Dunne FP. 2022. Twin boundary fatigue crack nucleation in a polycrystalline nickel superalloy containing non-metallic inclusions. *J. Mech. Phys. Solids* 160:104785
52. Poissant J, Barthelat F. 2010. A novel "subset splitting" procedure for digital image correlation on discontinuous displacement fields. *Exp. Mech.* 50:353–64
53. Réthoré J, Hild F, Roux S. 2007. Shear-band capturing using a multiscale extended digital image correlation technique. *Comput. Methods Appl. Mech. Eng.* 196:5016–30
54. Valle V, Hedan S, Cosenza P, Fauchille AL, Berdjane M. 2015. Digital image correlation development for the study of materials including multiple crossing cracks. *Exp. Mech.* 55:379–91
55. Stinville JC, Hestroffer JM, Charpagne MA, Polonsky AT, Echlin MP, et al. 2022. Multi-modal dataset of a polycrystalline metallic material: 3D microstructure and deformation fields. *Sci. Data* 9:460
56. Hestroffer JM, Latypov MI, Stinville JC, Charpagne MA, Valle V, et al. 2022. Development of grain-scale slip activity and lattice rotation fields in Inconel 718. *Acta Mater.* 226:117627
57. Stinville J, Lenthe W, Miao J, Pollock T. 2016. A combined grain scale elastic–plastic criterion for identification of fatigue crack initiation sites in a twin containing polycrystalline nickel-base superalloy. *Acta Mater.* 103:461–73
58. Stinville J, Charpagne M, Bourdin F, Callahan P, Chen Z, et al. 2020. Measurement of elastic and rotation fields during irreversible deformation using heaviside-digital image correlation. *Mater. Charact.* 169:110600
59. Echlin MP, Stinville JC, Miller VM, Lenthe WC, Pollock TM. 2016. Incipient slip and long range plastic strain localization in microtextured Ti-6Al-4V titanium. *Acta Mater.* 114:164–75
60. Hémery S, Naït-Ali A, Guéguen M, Wendorf J, Polonsky A, et al. 2019. A 3D analysis of the onset of slip activity in relation to the degree of micro-texture in Ti–6Al–4V. *Acta Mater.* 181:36–48
61. Wilkinson AJ, Hirsch PB. 1997. Electron diffraction based techniques in scanning electron microscopy of bulk materials. *Micron* 28:279–308
62. Cazottes S, Bechis A, Lafond C, L'Hôte G, Roth C, et al. 2019. Toward an automated tool for dislocation density characterization in a scanning electron microscope. *Mater. Charact.* 158:109954
63. Callahan PG, Haidet BB, Jung D, Seward GGE, Mukherjee K. 2018. Direct observation of recombination-enhanced dislocation glide in heteroepitaxial GaAs on silicon. *Phys. Rev. Mater.* 2:081601
64. Steinmetz DR, Jäpel T, Wietbrock B, Eisenlohr P, Gutierrez-Urrutia I, et al. 2013. Revealing the strain-hardening behavior of twinning-induced plasticity steels: theory, simulations, experiments. *Acta Mater.* 61:494–510
65. Simkin B, Crimp M, Bieler T. 2003. A factor to predict microcrack nucleation at γ–γ grain boundaries in TiAl. *Scr. Mater.* 49:149–54
66. Crimp MA. 2006. Scanning electron microscopy imaging of dislocations in bulk materials, using electron channeling contrast. *Microsc. Res. Tech.* 69:374–81
67. Ram F, Li Z, Zaefferer S, Hafez Haghighat SM, Zhu Z, et al. 2016. On the origin of creep dislocations in a Ni-base, single-crystal superalloy: an ECCI, EBSD, and dislocation dynamics-based study. *Acta Mater.* 109:151–61
68. Zauter R, Petry F, Bayerlein M, Sommer C, Christ HJ, Mughrabi H. 1992. Electron channelling contrast as a supplementary method for microstructural investigations in deformed metals. *Philos. Mag. A* 66:425–36
69. Ahmed J, Wilkinson A, Roberts S. 1997. Characterizing dislocation structures in bulk fatigued copper single crystals using electron channelling contrast imaging (ECCI). *Philos. Mag. Lett.* 76:237–46
70. Kaneko Y, Fukui K, Hashimoto S. 2005. Electron channeling contrast imaging of dislocation structures in fatigued austenitic stainless steels. *Mater. Sci. Eng. A* 400–401:413–17
71. L'Hôte G, Cazottes S, Lachambre J, Montagnat M, Courtois P, et al. 2019. Dislocation dynamics during cyclic loading in copper single crystal. *Materialia* 8:100501
72. Li Z, Tasan CC, Pradeep KG, Raabe D. 2017. A trip-assisted dual-phase high-entropy alloy: grain size and phase fraction effects on deformation behavior. *Acta Mater.* 131:323–35
73. Grilli N, Janssens K, Nellessen J, Sandlöbes S, Raabe D. 2018. Multiple slip dislocation patterning in a dislocation-based crystal plasticity finite element method. *Int. J. Plast.* 100:104–21

74. Callahan PG, Stinville JC, Yao ER, Echlin MP, Titus MS, et al. 2018. Transmission scanning electron microscopy: defect observations and image simulations. *Ultramicroscopy* 186:49–61
75. Gianola DS, Britton TB, Zaefferer S. 2019. New techniques for imaging and identifying defects in electron microscopy. *MRS Bull.* 44:450–58
76. Stinville J, Yao ER, Callahan PG, Shin J, Wang F, et al. 2019. Dislocation dynamics in a nickel-based superalloy via in-situ transmission scanning electron microscopy. *Acta Mater.* 168:152–66
77. Phillips P, Brandes M, Mills M, De Graef M. 2011. Diffraction contrast STEM of dislocations: imaging and simulations. *Ultramicroscopy* 111:1483–87
78. Wang F, Balbus GH, Xu S, Su Y, Shin J, et al. 2020. Multiplicity of dislocation pathways in a refractory multiprincipal element alloy. *Science* 370:95–101
79. Levin BDA. 2021. Direct detectors and their applications in electron microscopy for materials science. *J. Phys. Mater.* 4:042005
80. Wang F, Echlin MP, Taylor AA, Shin J, Bammes B, et al. 2021. Electron backscattered diffraction using a new monolithic direct detector: high resolution and fast acquisition. *Ultramicroscopy* 220:113160
81. Wilkinson AJ, Moldovan G, Britton TB, Bewick A, Clough R, Kirkland AI. 2013. Direct detection of electron backscatter diffraction patterns. *Phys. Rev. Lett.* 111:065506
82. Mingard K, Stewart M, Gee M, Vespucci S, Trager-Cowan C. 2018. Practical application of direct electron detectors to EBSD mapping in 2D and 3D. *Ultramicroscopy* 184:242–51
83. Kacher J, Ruggles T, Key J, Nowell M, Wright S. 2022. Characterizing defect structures in AM steel using direct electron detection EBSD. *Scr. Mater.* 221:114952
84. Echlin MP, Polonsky AT, Lamb J, Geurts R, Randolph SJ, et al. 2021. Recent developments in femtosecond laser-enabled TriBeam systems. *JOM* 73:4258–69
85. Rowenhorst DJ, Nguyen L, Murphy-Leonard AD, Fonda RW. 2020. Characterization of microstructure in additively manufactured 316L using automated serial sectioning. *Curr. Opin. Solid State Mater. Sci.* 24:100819
86. Echlin MP, Burnett TL, Polonsky AT, Pollock TM, Withers PJ. 2020. Serial sectioning in the SEM for three dimensional materials science. *Curr. Opin. Solid State Mater. Sci.* 24:100817
87. Zhu C, De Graef M. 2020. EBSD pattern simulations for an interaction volume containing lattice defects. *Ultramicroscopy* 218:113088
88. Wang F, Stinville JC, Charpagne M, Echlin MP, Agnew SR, et al. 2023. Dislocation cells in additively manufactured metallic alloys characterized by electron backscatter diffraction pattern sharpness. *Mater. Charact.* 197:112673
89. Witzen WA, Echlin MP, Charpagne MA, Pollock TM, Beyerlein IJ. 2023. Subgrain geometrically necessary dislocation density mapping in spalled Ta in three dimensions. *Acta Mater.* 244:118366
90. Witzen WA, Polonsky AT, Pollock TM, Beyerlein IJ. 2020. Three-dimensional maps of geometrically necessary dislocation densities in additively manufactured Ni-based superalloy IN718. *Int. J. Plast.* 131:102709
91. Jiang J, Britton T, Wilkinson A. 2013. Measurement of geometrically necessary dislocation density with high resolution electron backscatter diffraction: effects of detector binning and step size. *Ultramicroscopy* 125:1–9
92. Steinmetz DR, Zaefferer S. 2010. Towards ultrahigh resolution EBSD by low accelerating voltage. *Mater. Sci. Technol.* 26:640–45
93. Adhyaksa GWP, Brittman S, Āboliņš H, Lof A, Li X, et al. 2018. Understanding detrimental and beneficial grain boundary effects in halide perovskites. *Adv. Mater.* 30:1804792
94. Fonda RW, Spanos G. 2014. Effects of cooling rate on transformations in a Fe-9 pct Ni steel. *Metall. Mater. Trans. A* 45:5982–89
95. Trimby PW, Cao Y, Chen Z, Han S, Hemker KJ, et al. 2014. Characterizing deformed ultrafine-grained and nanocrystalline materials using transmission kikuchi diffraction in a scanning electron microscope. *Acta Mater.* 62:69–80
96. Singh S, Guo Y, Winiarski B, Burnett TL, Withers PJ, De Graef M. 2018. High resolution low kV EBSD of heavily deformed and nanocrystalline aluminium by dictionary-based indexing. *Sci. Rep.* 8:10991

97. Morales-Rivas L, Ram F, Spriestersbach D, Sippel J, De Graef M, Kerscher E. 2021. Fine granular area linked to very high cycle fatigue in martensitic and bainitic steels: characterization by means of EBSD-dictionary indexing. *Scr. Mater.* 194:113644
98. Zeisl S, Lassnig A, Hohenwarter A, Mendez-Martin F. 2022. Precipitation behavior of a Co-free Fe-Ni-Cr-Mo-Ti-Al maraging steel after severe plastic deformation. *Mater. Sci. Eng. A* 833:142416
99. Liao Z, Polyakov M, Diaz OG, Axinte D, Mohanty G, et al. 2019. Grain refinement mechanism of nickel-based superalloy by severe plastic deformation - mechanical machining case. *Acta Mater*. 180:2–14
100. Lenthe WC, Echlin MP, Stinville JC, De Graef M, Pollock TM. 2020. Twin related domain networks in René 88DT. *Mater. Charact.* 165:110365
101. Stinville JC, Martin E, Karadge M, Ismonov S, Soare M, et al. 2018. Competing modes for crack initiation from non-metallic inclusions and intrinsic microstructural features during fatigue in a polycrystalline nickel-based superalloy. *Metall. Mater. Trans. A* 49:3865–73
102. Lenthe WC, Stinville JC, Echlin MP, Pollock TM. 2016. Statistical assessment of fatigue-initiating microstructural features in a polycrystalline disk alloy. In *Superalloys 2016: Proceedings of the 13th International Symposium of Superalloys*, ed. M Hardy, E Huron, U Glatze, B Griffin, B Lewis, et al., pp. 567–78. Hoboken, NJ: John Wiley & Sons
103. Wilkinson AJ, Meaden G, Dingley DJ. 2006. High resolution mapping of strains and rotations using electron backscatter diffraction. *Mater. Sci. Technol.* 22:1271–78
104. Britton T, Wilkinson A. 2011. Measurement of residual elastic strain and lattice rotations with high resolution electron backscatter diffraction. *Ultramicroscopy* 111:1395–404
105. Villechaise P, Cormier J, Billot T, Mendez J. 2012. Mechanical behavior and damage processes of Udimet 720Li: influence of localized plasticity at grain boundaries. In *Superalloys 2012: Proceedings of the 12th International Symposium on Superalloys*, ed. ES Huron, RC Reed, MC Hardy, MJ Mills, RE Montero, et al., pp. 15–24. Hoboken, NJ: John Wiley & Sons
106. Larrouy B, Villechaise P, Cormier J, Berteaux O. 2015. Grain boundary–slip bands interactions: impact on the fatigue crack initiation in a polycrystalline forged Ni-based superalloy. *Acta Mater*. 99:325–36
107. Koko A, Elmukashfi E, Becker TH, Karamched PS, Wilkinson AJ, Marrow TJ. 2022. In situ characterisation of the strain fields of intragranular slip bands in ferrite by high-resolution electron backscatter diffraction. *Acta Mater*. 239:118284
108. Guo Y, Collins D, Tarleton E, Hofmann F, Tischler J, et al. 2015. Measurements of stress fields near a grain boundary: exploring blocked arrays of dislocations in 3D. *Acta Mater*. 96:229–36
109. Danilewsky AN. 2020. X-ray topography—more than nice pictures. *Cryst. Res. Technol.* 55:2000012
110. Cho A. 2020. X-ray source gets a 100-fold boost in brightness. *Science* 369:234–35
111. Ludwig W, Lauridsen EM, Schmidt S, Poulsen HF, Baruchel J. 2007. High-resolution three-dimensional mapping of individual grains in polycrystals by topotomography. *J. Appl. Crystallogr.* 40:905–11
112. Hänschke D, Helfen L, Altapova V, Danilewsky A, Baumbach T. 2012. Three-dimensional imaging of dislocations by X-ray diffraction laminography. *Appl. Phys. Lett.* 101:244103
113. Viganò N, Ludwig W. 2020. X-ray orientation microscopy using topo-tomography and multi-mode diffraction contrast tomography. *Curr. Opin. Solid State Mater. Sci.* 24:100832
114. Proudhon H, Pelerin M, King A, Ludwig W. 2020. In situ 4D mechanical testing of structural materials: the data challenge. *Curr. Opin. Solid State Mater. Sci.* 24:100834
115. Gustafson S, Ludwig W, Shade P, Naragani D, Pagan D, et al. 2020. Quantifying microscale drivers for fatigue failure via coupled synchrotron X-ray characterization and simulations. *Nat. Commun.* 11:3189
116. Simons H, King A, Ludwig W, Detlefs C, Pantleon W, et al. 2015. Dark-field X-ray microscopy for multiscale structural characterization. *Nat. Commun.* 6:6098
117. Jakobsen AC, Simons H, Ludwig W, Yildirim C, Leemreize H, et al. 2019. Mapping of individual dislocations with dark-field X-ray microscopy. *J. Appl. Crystallogr.* 52:122–32
118. Dresselhaus-Marais LE, Winther G, Howard M, Gonzalez A, Breckling SR, et al. 2021. In situ visualization of long-range defect interactions at the edge of melting. *Sci. Adv.* 7:eabe8311
119. Porz L, Klomp AJ, Fang X, Li N, Yildirim C, et al. 2021. Dislocation-toughened ceramics. *Mater. Horiz.* 8:1528–37

120. Yildirim C, Mavrikakis N, Cook P, Rodriguez-Lamas R, Kutsal M, et al. 2022. 4D microstructural evolution in a heavily deformed ferritic alloy: a new perspective in recrystallisation studies. *Scr. Mater.* 214:114689
121. Kutsal M, Bernard P, Berruyer G, Cook PK, Hino R, et al. 2019. The ESRF dark-field X-ray microscope at ID06. *IOP Conf. Ser. Mater. Sci. Eng.* 580:012007
122. Wright J, Giacobbe C, Majkut M. 2020. New opportunities at the materials science beamline at ESRF to exploit high energy nano-focus X-ray beams. *Curr. Opin. Solid State Mater. Sci.* 24:100818
123. Ice GE, Pang JWL, Larson BC, Budai JD, Tischler JZ, et al. 2009. At the limit of polychromatic microdiffraction. *Mater. Sci. Eng. A* 524:3–9
124. Liu W, Ice GE, Assoufid L, Liu C, Shi B, et al. 2011. Achromatic nested Kirkpatrick–Baez mirror optics for hard X-ray nanofocusing. *J. Synchrotron Radiat.* 18:575–79
125. Larson BC, Yang W, Ice GE, Budai JD, Tischler JZ. 2002. Three-dimensional X-ray structural microscopy with submicrometre resolution. *Nature* 415:887–90
126. Li R, Xie Q, Wang YD, Liu W, Wang M, et al. 2017. Unraveling submicron-scale mechanical heterogeneity by three-dimensional X-ray microdiffraction. *PNAS* 115:483–88
127. Bonnin A, Wright JP, Tucoulou R, Palancher H. 2014. Impurity precipitation in atomized particles evidenced by nano X-ray diffraction computed tomography. *Appl. Phys. Lett.* 105:084103
128. Hayashi Y, Setoyama D, Hirose Y, Yoshida T, Kimura H. 2019. Intragranular three-dimensional stress tensor fields in plastically deformed polycrystals. *Science* 366:1492–96
129. Henningsson NA, Hall SA, Wright JP, Hektor J. 2020. Reconstructing intragranular strain fields in polycrystalline materials from scanning 3DXRD data. *J. Appl. Crystallogr.* 53:314–25
130. Henningsson A, Hendriks J. 2021. Intragranular strain estimation in far-field scanning X-ray diffraction using a Gaussian process. *J. Appl. Crystallogr.* 54:1057–70
131. Liu J, Vanderesse N, Stinville JC, Pollock T, Bocher P, Texier D. 2019. In-plane and out-of-plane deformation at the sub-grain scale in polycrystalline materials assessed by confocal microscopy. *Acta Mater.* 169:260–74
132. Wei S, Kim J, Tasan CC. 2022. In-situ investigation of plasticity in a Ti-Al-V-Fe ($\alpha+\beta$) alloy: Slip mechanisms, strain localization, and partitioning. *Int. J. Plast.* 148:103131
133. Dichtl C, Lunt D, Atkinson M, Thomas R, Plowman A, et al. 2022. Slip activity during low-stress cold creep deformation in a near-α titanium alloy. *Acta Mater.* 229:117691
134. Lim H, Carroll JD, Michael JR, Battaile CC, Chen SR, Lane JMD. 2020. Investigating active slip planes in tantalum under compressive load: crystal plasticity and slip trace analyses of single crystals. *Acta Mater.* 185:1–12
135. Luan Q, Xing H, Zhang J, Jiang J. 2020. Experimental and crystal plasticity study on deformation bands in single crystal and multi-crystal pure aluminium. *Acta Mater.* 183:78–92
136. Yang Y, Wang L, Bieler TR, Eisenlohr P, Crimp MA. 2011. Quantitative atomic force microscopy characterization and crystal plasticity finite element modeling of heterogeneous deformation in commercial purity titanium. *Metall. Mater. Trans. A* 42:636–44
137. Chen Z, Lenthe W, Stinville JC, Echlin M, Pollock TM, Daly S. 2018. High-resolution deformation mapping across large fields of view using scanning electron microscopy and digital image correlation. *Exp. Mech.* 58:1407–21
138. Charpagne MA, Stinville JC, Polonsky AT, Echlin MP, Murray SP, et al. 2020. Tuning strain localization in polycrystalline nickel-based superalloys by thermomechanical processing. In *Superalloys 2020: Proceedings of the 14th International Symposium on Superalloys*, ed. S Tin, M Hardy, J Clews, J Cormier, Q Feng, et al., pp. 471–81. Cham, Switz.: Springer Int.
139. Nolze G. 2007. Image distortions in SEM and their influences on EBSD measurements. *Ultramicroscopy* 107:172–83
140. Charpagne MA, Strub F, Pollock TM. 2019. Accurate reconstruction of EBSD datasets by a multimodal data approach using an evolutionary algorithm. *Mater. Charact.* 150:184–98
141. Winiarski B, Gholinia A, Mingard K, Gee M, Thompson G, Withers P. 2021. Correction of artefacts associated with large area EBSD. *Ultramicroscopy* 226:113315
142. Nguyen LT, Rowenhorst DJ. 2021. The alignment and fusion of multimodal 3D serial sectioning datasets. *JOM* 73:3272–84

143. Tong VS, Ben Britton T. 2021. TrueEBSD: Correcting spatial distortions in electron backscatter diffraction maps. *Ultramicroscopy* 221:113130
144. Liang D, Hure J, Courcelle A, Shawish SE, Tanguy B. 2021. A micromechanical analysis of intergranular stress corrosion cracking of an irradiated austenitic stainless steel. *Acta Mater*. 204:116482
145. Ånes HW, van Helvoort ATJ, Marthinsen K. 2022. Correlated subgrain and particle analysis of a recovered Al-Mn alloy by directly combining EBSD and backscatter electron imaging. *Mater. Charact.* 193:112228
146. Zhang Y, Elbrønd A, Lin F. 2014. A method to correct coordinate distortion in EBSD maps. *Mater. Charact.* 96:158–65
147. Polonsky AT, Raghavan N, Echlin MP, Kirka MM, Dehoff RR, Pollock TM. 2020. 3D characterization of the columnar-to-equiaxed transition in additively manufactured Inconel 718. In *Superalloys 2020: Proceedings of the 14th International Symposium on Superalloys*, ed. S Tin, M Hardy, J Clews, J Cormier, Q Feng, et al., pp. 990–1002. Cham, Switz.: Springer Int.
148. Chen Z, Daly S. 2020. Automated identification of deformation twin systems in Mg WE43 from SEM DIC. *Mater. Charact.* 169:110628
149. Charpagne M, Stinville J, Polonsky A, Echlin M, Pollock T. 2021. A multi-modal data merging framework for correlative investigation of strain localization in three dimensions. *JOM* 73:3263–71
150. Groeber MA, Jackson MA. 2014. DREAM.3D: A digital representation environment for the analysis of microstructure in 3D. *Integrat. Mater. Manuf. Innov.* 3:56–72
151. Proudhon H. 2022. Pymicro. *Github*. **https://github.com/heprom/pymicro**
152. Charpagne M, Stinville J, Callahan P, Texier D, Chen Z, et al. 2020. Automated and quantitative analysis of plastic strain localization via multi-modal data recombination. *Mater. Charact.* 163:110245
153. Bridier F, Villechaise P, Mendez J. 2005. Analysis of the different slip systems activated by tension in a α/β titanium alloy in relation with local crystallographic orientation. *Acta Mater*. 53:555–67
154. Bayerschen E, McBride A, Reddy B, Böhlke T. 2016. Review on slip transmission criteria in experiments and crystal plasticity models. *J. Mater. Sci.* 51:2243–58
155. Alizadeh R, Peña-Ortega M, Bieler T, LLorca J. 2020. A criterion for slip transfer at grain boundaries in Al. *Scr. Mater.* 178:408–12
156. Bieler T, Alizadeh R, Peña-Ortega M, LLorca J. 2019. An analysis of (the lack of) slip transfer between near-cube oriented grains in pure Al. *Int. J. Plast.* 118:269–90
157. Zhao Z, Bieler TR, LLorca J, Eisenlohr P. 2020. Grain boundary slip transfer classification and metric selection with artificial neural networks. *Scr. Mater.* 185:71–75
158. Vermeij T, Peerlings RHJ, Geers MGD, Hoefnagels JPM. 2023. Automated identification of slip system activity fields from digital image correlation data. *Acta Mater*. 243:118502
159. Charpagne M, Stinville J, Wang F, Philips N, Pollock T. 2022. Orientation dependent plastic localization in the refractory high entropy alloy HfNbTaTiZr at room temperature. *Mater. Sci. Eng. A* 848:143291
160. Schmid E, Valouch MA. 1932. About the sudden translation of zinc crystals. *Z. Phys.* 75:531–38
161. Becker R, Orowan E. 1932. Sudden expansion of zinc crystals. *Z. Phys.* 79:566–72
162. Tinder RF, Trzil JP. 1973. Millimicroplastic burst phenomena in zinc monocrystals. *Acta Metall.* 21:975–89
163. Chatterjee K, Beaudoin AJ, Pagan DC, Shade PA, Philipp HT, et al. 2019. Intermittent plasticity in individual grains: a study using high energy X-ray diffraction. *Struct. Dyn.* 6:014501
164. Deschanel S, Ben Rhouma W, Weiss J. 2017. Acoustic emission multiplets as early warnings of fatigue failure in metallic materials. *Sci. Rep.* 7:13680
165. Csikor FF, Motz C, Weygand D, Zaiser M, Zapperi S. 2007. Dislocation avalanches, strain bursts, and the problem of plastic forming at the micrometer scale. *Science* 318:251–54
166. Rizzardi Q, McElfresh C, Sparks G, Stauffer DD, Marian J, Maass R. 2022. Mild-to-wild plastic transition is governed by athermal screw dislocation slip in bcc Nb. *Nat. Commun.* 13:1010
167. Schuh CA. 2006. Nanoindentation studies of materials. *Mater. Today* 9:32–40
168. Uchic MD, Shade P, Dimiduk DM. 2009. Plasticity of micrometer-scale single-crystals in compression. *Annu. Rev. Mater. Res.* 39:361–86
169. Pharr GM, Herbert EG, Gao Y. 2010. The indentation size effect: a critical examination of experimental observations and mechanistic interpretations. *Annu. Rev. Mater. Res.* 40:271–92

170. Shimanek J, Rizzardi Q, Sparks G, Derlet PM, Maass R. 2020. Scale-dependent pop-ins in nanoindentation and scale-free plastic fluctuations in microcompression. *J. Mater. Res.* 35:196–205
171. Morris JR, Bei H, Pharr GM, George EP. 2011. Size effects and stochastic behavior of nanoindentation pop in. *Phys. Rev. Lett.* 106:165502
172. Gerberich WW, Nelson JC, Lilleodden ET, Anderson P, Wyrobek JT. 1996. Indentation induced dislocation nucleation: the initial yield point. *Acta Mater.* 44:3585–98
173. Zhang L, Ohmura T. 2014. Plasticity initiation and evolution during nanoindentation of an iron-3% silicon crystal. *Phys. Rev. Lett.* 112:145504
174. Lilleodden ET, Nix WD. 2006. Microstructural length-scale effects in the nanoindentation behavior of thin gold films. *Acta Mater.* 54:1583–93
175. Schuh CA, Mason JK, Lund AC. 2005. Quantitative insight into dislocation nucleation from high-temperature nanoindentation experiments. *Nat. Mater.* 4:617–21
176. Perepezko JH, Imhoff SD, Chen MW, Wang JQ, Gonzalez S. 2014. Nucleation of shear bands in amorphous alloys. *PNAS* 111:3938–42
177. Tönnies D, Samwer K, Derlet PM, Volkert CA, Maass R. 2015. Rate-dependent shear-band initiation in a metallic glass. *Appl. Phys. Lett.* 106:171907
178. Derlet PM, Maass R. 2016. The stress statistics of the first pop-in or discrete plastic event in crystal plasticity. *J. Appl. Phys.* 120:225101
179. Li J, Kirchlechner C. 2020. Does the stacking fault energy affect dislocation multiplication? *Mater. Charact.* 161:110136
180. Schuh CA, Argon AS, Nieh TG, Wadsworth J. 2003. The transition from localized to homogeneous plasticity during nanoindentation of an amorphous metal. *Philos. Mag.* 83:2585–97
181. Gan B, Tin S. 2012. Phenomenological description and temperature dependence of serrated flow in Ni–10Pd during high temperature instrumented microindentation. *Mater. Sci. Eng. A* 554:41–47
182. Ikeda Y, Mancias J, Gan B, Maass R. 2021. Evidence of room-temperature shear-deformation in a Cu-Al intermetallic. *Scr. Mater.* 190:126–30
183. Packard CE, Schuh CA. 2007. Initiation of shear bands near a stress concentration in metallic glass. *Acta Mater.* 55:5348–58
184. Hintsala ED, Hangen U, Stauffer DD. 2018. High-throughput nanoindentation for statistical and spatial property determination. *JOM* 70:494–503
185. Chang Y, Lin M, Hangen U, Richter S, Haase C, Bleck W. 2021. Revealing the relation between microstructural heterogeneities and local mechanical properties of complex-phase steel by correlative electron microscopy and nanoindentation characterization. *Mater. Des.* 203:109620
186. Koumoulos EP, Paraskevoudis K, Charitidis CA. 2019. Constituents phase reconstruction through applied machine learning in nanoindentation mapping data of mortar surface. *J. Compos. Sci.* 3:63
187. McCue I, Gaskey B, Crawford B, Erlebacher J. 2016. Local heterogeneity in the mechanical properties of bicontinuous composites made by liquid metal dealloying. *Appl. Phys. Lett.* 109:231901
188. Chang HW, Zhang MX, Atrens A, Huang H. 2014. Nanomechanical properties of Mg–Al intermetallic compounds produced by packed powder diffusion coating (PPDC) on the surface of AZ91E. *J. Alloys Compd.* 587:527–32
189. Lilleodden ET, Zimmerman JA, Foiles SM, Nix WD. 2003. Atomistic simulations of elastic deformation and dislocation nucleation during nanoindentation. *J. Mech. Phys. Solids* 51:901–20
190. Konstantopoulos G, Koumoulos EP, Charitidis CA. 2020. Classification of mechanism of reinforcement in the fiber-matrix interface: application of machine learning on nanoindentation data. *Mater. Des.* 192:108705
191. Lu L, Dao M, Kumar P, Ramamurty U, Karniadakis GE, Suresh S. 2020. Extraction of mechanical properties of materials through deep learning from instrumented indentation. *PNAS* 117:7052
192. Uchic MD, Dimiduk DM, Florando JN, Nix WD. 2004. Sample dimensions influence strength and crystal plasticity. *Science* 305:986–89
193. Jennings AT, Li J, Greer JR. 2011. Emergence of strain-rate sensitivity in Cu nanopillars: transition from dislocation multiplication to dislocation nucleation. *Acta Mater.* 59:5627–37

194. Xiao Y, Kozak R, Haché MJ, Steurer W, Spolenak R, et al. 2020. Micro-compression studies of face-centered cubic and body-centered cubic high-entropy alloys: size-dependent strength, strain rate sensitivity, and activation volumes. *Mater. Sci. Eng. A* 790:139429
195. Wheeler J, Thilly L, Morel A, Taylor A, Montagne A, et al. 2016. The plasticity of indium antimonide: insights from variable temperature, strain rate jump micro-compression testing. *Acta Mater*. 106:283–89
196. Ispánovity PD, Hegyi Á, Groma I, Györgyi G, Ratter K, Weygand D. 2013. Average yielding and weakest link statistics in micron-scale plasticity. *Acta Mater*. 61:6234–45
197. Dimiduk DM, Woodward C, LeSar R, Uchic MD. 2006. Scale-free intermittent flow in crystal plasticity. *Science* 312:1188–90
198. Sethna JP, Bierbaum MK, Dahmen KA, Goodrich CP, Greer JR, et al. 2017. Deformation of crystals: connections with statistical physics. *Annu. Rev. Mater. Res.* 47:217–46
199. Sparks G, Maass R. 2019. Effects of orientation and pre-deformation on velocity profiles of dislocation avalanches in gold microcrystals. *Eur. Phys. J. B* 92:15
200. Sparks G, Maass R. 2018. Nontrivial scaling exponents of dislocation avalanches in microplasticity. *Phys. Rev. Mater.* 2:120601
201. Krebs J, Rao SI, Verheyden S, Miko C, Goodall R, et al. 2017. Cast aluminium single crystals cross the threshold from bulk to size-dependent stochastic plasticity. *Nat. Mater.* 16:730–736
202. Rizzardi Q, Derlet PM, Maaß R. 2022. Intermittent microplasticity in the presence of a complex microstructure. *Phys. Rev. Mater.* 6:073602
203. Sparks G, Maaß R. 2018. Shapes and velocity relaxation of dislocation avalanches in Au and Nb microcrystals. *Acta Mater*. 152:86–95
204. Rizzardi Q, Sparks G, Maaß R. 2018. Fast slip velocity in a high-entropy alloy. *JOM* 70:1088–93
205. Sparks G, Cui Y, Po G, Rizzardi Q, Marian J, Maass R. 2019. Avalanche statistics and the intermittent-to-smooth transition in microplasticity. *Phys. Rev. Mater.* 3:080601
206. Maass R, Klaumünzer D, Löffler JF. 2011. Propagation dynamics of individual shear bands during inhomogeneous flow in a Zr-based bulk metallic glass. *Acta Mater*. 59:3205–13
207. Shashkov I, Lebyodkin M, Lebedkina T. 2012. Multiscale study of acoustic emission during smooth and jerky flow in an AlMg alloy. *Acta Mater*. 60:6842–50
208. Sparks G, Phani PS, Hangen U, Maass R. 2017. Spatiotemporal slip dynamics during deformation of gold micro-crystals. *Acta Mater*. 122:109–19
209. Kubin LP, Jouffrey B. 1973. Etude de la déformation plastique de monocristaux de niobium de haute pureté a basse température. *Philos. Mag. A* 27:1369–85
210. Rizzardi Q, Derlet PM, Maass R. 2021. Microstructural signatures of dislocation avalanches in a high-entropy alloy. *Phys. Rev. Mater.* 5:043604
211. Weiss J, Ben Rhouma W, Deschanel S, Truskinovsky L. 2019. Plastic intermittency during cyclic loading: from dislocation patterning to microcrack initiation. *Phys. Rev. Mater.* 3:023603
212. Zhao X, Strickland DJ, Derlet PM, He M-R, Cheng YJ, et al. 2015. In situ measurements of a homogeneous to heterogeneous transition in the plastic response of ion-irradiated ⟨111⟩ Ni microspecimens. *Acta Mater*. 88:121–35
213. Chatterjee K, Beaudoin AJ, Pagan DC, Shade PA, Philipp HT, et al. 2019. Intermittent plasticity in individual grains: a study using high energy X-ray diffraction. *Struct. Dyn.* 6:014501
214. Zhang P, Bian JJ, Zhang JY, Liu G, Weiss J, Sun J. 2020. Plate-like precipitate effects on plasticity of Al-Cu alloys at micrometer to sub-micrometer scales. *Mater. Des.* 188:108444
215. Beyerlein IJ, Knezevic M. 2018. Mesoscale, microstructure-sensitive modeling for interface-dominated, nanostructured materials. In *Handbook of Materials Modeling*, ed. W Andreoni, S Yip, pp. 1111–52. Cham, Switz.: Springer Int.
216. Kumar MA, Beyerlein IJ. 2020. Local microstructure and micromechanical stress evolution during deformation twinning in hexagonal polycrystals. *J. Mater. Res.* 35:217–41
217. Zhang M, Bridier F, Villechaise P, Mendez J, McDowell D. 2010. Simulation of slip band evolution in duplex Ti–6Al–4V. *Acta Mater*. 58:1087–96
218. Ahmadikia B, Kumar MA, Beyerlein IJ. 2021. Effect of neighboring grain orientation on strain localization in slip bands in HCP materials. *Int. J. Plast.* 144:103026

219. Beyerlein IJ, Zhang X, Misra A. 2014. Growth twins and deformation twins in metals. *Annu. Rev. Mater. Res.* 44:329–63
220. Jiang J, Dunne FPE, Britton TB. 2017. Toward predictive understanding of fatigue crack nucleation in Ni-based superalloys. *JOM* 69:863–71
221. Latypov MI, Hestroffer JM, Stinville JC, Mayeur JR, Pollock TM, Beyerlein IJ. 2021. Modeling lattice rotation fields from discrete crystallographic slip bands in superalloys. *Extreme Mech. Lett.* 49:101468
222. Wang L, Yang Y, Eisenlohr P, Bieler T, Crimp M, Mason D. 2009. Twin nucleation by slip transfer across grain boundaries in commercial purity titanium. *Metall. Mater. Trans. A* 41:421–30
223. Kumar MA, Beyerlein IJ. 2020. Influence of plastic properties on the grain size effect on twinning in Ti and Mg. *Mater. Sci. Eng. A* 771:138644
223a. Black RL, Garbowski T, Bean C, Eberle AL, Nickell S, et al. 2023. High-throughput high-resolution digital image correlation measurements by multi-beam SEM imaging. *Exp. Mech*. In press. **https://doi.org/10.1007/s11340-023-00961-y**
224. Yildirim C, Poulsen HF, Winther G, Detlefs C, Huang PH, Dresselhaus-Marais LE. 2023. Extensive 3D mapping of dislocation structures in bulk aluminum. *Sci. Rep.* 13:3834
225. Durmaz AR, Hadzic N, Straub T, Eberl C, Gumbsch P. 2021. Efficient experimental and data-centered workflow for microstructure-based fatigue data. *Exp. Mech.* 61:1489–502
226. Alcalá J, Očenášek J, Varillas J, A. El-Awady J, Wheeler JM, Michler J. 2020. Statistics of dislocation avalanches in fcc and bcc metals: dislocation mechanisms and mean swept distances across microsample sizes and temperatures. *Sci. Rep.* 10:19024

Annual Review of Materials Research

Volume 53, 2023

Contents